Accepted manuscript. Published in Géotechnique (2021). Version of record: https://doi.org/10.1680/jgeot.21.00126. This is the authors' final version after peer review. Please cite the published article.

Evidence of a Unique Critical Fabric Surface for Granular Soils

Yuxuan Wen[1] and Yida Zhang[2*]

ABSTRACT

The critical state of granular soils needs to make proper reference to the fabric that develops at critical state. This study substantializes the concept of critical fabric surface (CFS) which attracts the fabric state of granular soils upon continuous shearing. Numerical experiments using discrete element modelling (DEM) are conducted under drained and undrained conditions with varies Lode angles. Fabric tensors are defined based on the normals of all contacts and of the strong force contacts only. Both tensors have their spherical component preserved such that the information of coordination number can be carried. A separate series of low confining pressure undrained test are conducted to probe the fabric states of soils in the post-liquefaction regime. Finally, a single CFS spanning across a wide range of coordination numbers is established based on the DEM results. The CFS concept provides an important reference state for soils sheared to large strains in complementary to the traditionally defined critical state. It provides a new perspective to interpret and model the mechanics of granular soils in both pre- and post- liquefied regimes. The evolution of fabric shows that the normalized strong-contact fabric evolves linearly with the stress ratio even for liquefied or anisotropically consolidated soils.

KEYWORDS: Anisotropy, Discrete-element modelling, Fabric/structure of soils, Liquefaction, Sands

[1] Graduate student, Department of Civil, Environmental and Architectural Engineering, University of Colorado Boulder, Boulder, CO, USA

[2] Assistant Professor, Department of Civil, Environmental and Architectural Engineering, University of Colorado Boulder, Boulder, CO, USA. Email: yida.zhang@colorado.edu

INTRODUCTION

In modern soil mechanics, the critical state theory (CST) (Roscoe et al., 1958; Schofield & Wroth, 1968) is one of the major cornerstones that characterized the field. The theory states that the shear stress and the volume of soil reaches a critical state after sufficient shearing. Later, it was realized that fabric anisotropy which has a significant impact on the stress-strain response of soils (e.g., Nakata et al., 1998; Yoshimine et al., 1998) was not considered in the classical CST. A remediation is later proposed by Li & Dafalias (2012) by introducing an additional critical state condition related to the normalized anisotropic fabric tensor, which is referred to as the anisotropic critical state theory (ACST). The modelling of granular soils within the framework of ACST (Woo & Salgado, 2015; Dafalias and Taiebat, 2016; Gao & Zhao, 2017) is therefore necessary to deal with fabric anisotropy and fabric evolution, which has motivated numerous experimental studies enabled by X-ray microtomography (Fonseca et al., 2013a, 2013b; Wiebicke et al., 2017; Imseeh et al, 2018) and discrete element modelling (DEM) (Kuhn, 2010; Zhao & Guo, 2013; Fu & Dafalias, 2015; Kruyt & Rothenburg, 2016; Nguyen et al., 2017, 2018; Wang et al. 2017; Yang & Wu, 2017).

Given the difficulties and costs in experimental measurements of soil microstructure, DEM (Cundall & Strack, 1979) is still the main research tool to understand the fabric evolution of granular soils under quasi-static shearing. In these studies, fabric tensor could be quantified based on the statistics of certain intergranular attributes, using which the normalized fabric anisotropy (A) can be defined although its specific expression may vary. Zhao & Guo (2013) conducted a series of true triaxial DEM tests and found that, at critical state, A forms an inverted smoothed triangular surface on the fabric π-plane, reciprocal to the critical stress surface on the stress π-plane. Similar behaviour was also observed in Thornton & Zhang (2010) and Yimisiri & Soga (2010). Zhao & Guo (2013) also demonstrated that the first joint invariant (K) of the stress and fabric tensors at critical state is independent of Lode angle, leading to a new critical state line (CSL) in K-e-p space, where e is the void ratio and p is the mean effective stress. Fu & Dafalias (2011) reported the coordination number (CN) in their simulations and found there are unique CN-p and A-p relations at critical state, which

was also verified by Guo & Zhao (2013) and Nguyen et al. (2017, 2018). Combined with the classical CSL, this implies a unique fabric structure (A, CN, e) and stress state (p, q) is reached at the critical state. The interplay between soil fabric and liquefaction is also of great research interest lately. Guo & Zhao (2013) and Gu et al. (2014) found that CN drops drastically during shearing before liquefaction. Wang & Wei (2016) and Wang et al. (2016) observed that the variation of CN with respect to shear strain exhibits "butterfly" loops after the initial liquefaction in cyclic undrained test, meaning that CN is not a constant after initial liquefaction.

Despite these efforts, many questions regarding the fabric-stress-strain relation of soils remain unanswered. The results of Wang et al. (2016, 2019) indicate that soil fabric in the post liquefaction regime is not a constant but can vary within a limit range. A natural question follows: why such limit exists and how to quantify this limiting range of soil fabric? On the other hand, the similar but reciprocal shapes of the critical fabric envelop and the critical stress envelope on the π-plane makes one suspect some correlations exists between fabric and stress states. Indeed, it has been recently shown by Shi & Guo (2018) that a linear, Lode-angle and pressure independent relation exists between the strong-contact fabric tensor and the stress tensor for isotropically consolidated specimens (which will be simply referred to as the fabric evolution curve hereafter). Whether this linear relation is true for anisotropically consolidated specimens in pre- and post- liquified regimes still remains unknown. Besides, such relation for total-contact fabric tensor is not as straightforward and require further studies.

Another observation is that most DEM studies including the aforementioned works adopt the normalised anisotropic (traceless) fabric tensor to represent soil structures, by which the information of CN is invariably lost. Considering the new evidence showing that CN also reaches an ultimate value at critical state, it is plausible to use the full fabric tensor (the spherical component of which being the CN) in analysing the fabric data from DEM simulations. Zhang et al. (2020) showed that the use of the full fabric tensor permits one to construct a hypothetical critical fabric surface (CFS) in a three-dimensional (3D) principal

fabric space. Such surface can elegantly synthesize the previous observations on the *A*-*CN* relation at critical state and is consistent with the classical CST and ACST conditions if supplemented with additional constitutive relations.

Centred on the concept of CFS, a critical fabric theory (CFT) was recently developed and successfully applied to model the stress-strain behaviour of granular soils (Zhang et al., 2020). The proposed CFT, however, was based on hypotheses drawn from literatures that are mostly focused on normalized anisotropic fabric tensors. The concept of CFS based on the full fabric tensor has never been confirmed by experimental or DEM observations. To fill this gap, a series of DEM tests were conducted in this study, aiming at: 1) analysing the full fabric tensor at critical state and identifying a CFS in the principal fabric space; 2) investigating the fabric characteristics of sand in the post-liquefaction regime; 3) studying the fabric evolution curves for anisotropically consolidated specimens. First, the methodology of the study is introduced, including the DEM model, simulation parameters, testing conditions and fabric tensor definitions. Then the evolution of stress and fabric states under drained (constant p) and undrained true triaxial tests are presented. A separate series of undrained triaxial tests is followed to obtain the critical fabric states after liquefaction. Finally, the full dataset is mathematically represented by a single critical fabric surface. The fabric evolution curves obtained in this study are examined at last and discussed with reference to existing findings in the literature.

METHODOLOGY

DEM simulation

The open-source code YADE (Šmilauer et al., 2015) is used in this study for 3D DEM testing. The simulations are performed on a cubic representative elementary volume consists of 10,000 spherical particles with the particle size distribution shown in Fig. 1. Periodic boundaries are adopted to minimize boundary effects. Initially, an assembly of particles with no contact are generated and then isotropically (or K_0) consolidated to the desired value of p using a servo-control algorithm. The particle-particle friction coefficient μ in the

consolidation stage is adjusted to obtain different initial void ratio e_0. In the shearing stage, μ is updated to 0.5 which is typical for quartz sand (Thornton & Zhang, 2010; Guo & Zhao, 2013; Xie et al., 2017; Shi & Guo, 2018). The adopted values of μ at consolidation stage are less than 0.5 to ensure that the specimen is always stable after updated μ to 0.5 at the beginning of shearing. A linear force-displacement contact law is employed where the normal and the tangential stiffnesses of a particle with diameter d are set as $k_n / d = k_s / d = 100$ MPa. The normal and tangential stiffnesses of a contact between two particles are calculated as $K_n = k_{n1} \cdot k_{n2} / (k_{n1} + k_{n2})$, $K_s = k_{s1} \cdot k_{s2} / (k_{s1} + k_{s2})$ where k_{n1}, k_{s1} and k_{n2}, k_{s2} are the stiffness of two particles in contact, respectively. The normal and tangential contact forces are calculated by $F_n = K_n \delta_n$ and $F_s = K_s \delta_s$ with δ_n and δ_s being the normal and tangential displacements of the contact.

The particle density is scaled in this study to reduce computational cost (Thornton & Antony, 2000; Ng, 2006; Xie et al., 2017; Nguyen et al., 2017). Specifically, the particle density is scaled up from $\rho_g = 2.65 \times 10^3$ to 2.65×10^6 kg/m^3. This raises the critical time step $\Delta t_{cr} = \min_i \left(R_i \sqrt{(\rho_g)_i / E_i} \right)$ by a factor of $\sqrt{1000} = 31.62$, where R is the particle radius, E the Young's modulus, and subscript "i" represents the ith particle (Šmilauer et al., 2015). To ensure quasi-static loading condition, the inertial number $I = \dot{\varepsilon} \bar{d} \sqrt{\rho_g / p}$ should be smaller than 10^{-3} (Midi, 2004; da Cruze et al. 2005; Guo & Zhao, 2014; Lopera Perez et al., 2016) where $\dot{\varepsilon}$ is the strain rate, $\bar{d}$ the average particle diameter, and p the mean effective stress. In addition to ensuring $I << 10^{-3}$, quasi-static conditions were verified by performing a sensitivity analysis using different strain rates. Based on these considerations, a strain rate of 0.05 s^{-1} is selected for all simulations in this study

Four types of tests are conducted, two of which are the isotropically consolidated drained (CID) tests and isotropically consolidated undrained (CIU) tests. The CID and CIU tests are performed under a variety of confining pressures $p_0 = 50$, 100, 300, 500, 700, 1000, 1500 and 2000 kPa, aiming to identify the full CFS of this granular assembly across a wide range of coordination numbers. The initial void ratios e_0 of these tests prepared by isotropic

compression of an initially loose granular specimen with $\mu = 0.36$ are shown in Table 1. The CID tests are conducted under constant mean normal stress p with various intermediate principal stress ratios $b = 0$, 0.25, 0.5, 0.75 and 1. The CIU tests are performed under zero volumetric strain with various intermediate principal strain ratios $b_e = 0$, 0.25, 0.5, 0.75 and 1. Here $b = (\sigma_2 - \sigma_3)/(\sigma_1 - \sigma_3)$ and $b_e = (\varepsilon_2 - \varepsilon_3)/(\varepsilon_1 - \varepsilon_3)$, where $(\sigma_1, \sigma_2, \sigma_3)$ and $(\varepsilon_1, \varepsilon_2, \varepsilon_3)$ are the major, intermediate and minor principal stresses and strains, respectively. In addition, to check the uniqueness of the CFS obtained from CID and CIU tests, another series of CID test using two different initial void ratios at $p = 1000$ kPa, namely CID_e_0 tests, is performed. These specimens are prepared using $\mu = 0.2$ and 0.5 in the consolidation stage to generate initially denser and looser states, respectively. Finally, K_0 consolidated drained (CK_0D) tests are conducted with initial stress ratio $K_0 = \sigma_3 / \sigma_1 = 0.625$ and 0.75 under constant $p = 1000$ kPa to verify the uniqueness of CFS and examine fabric evolution when the specimen has some inherent fabric anisotropy. In total, 100 tests are conducted and the test conditions are summarized in Table 2. All specimens are sheared to a large value of axial strain $\varepsilon_a = 50\%$ to achieve the apparent critical state condition.

Fabric tensor definition

Soil fabric is a general concept and its mathematical description is not unique. Majority of the existing DEM studies describe soil microstructure via the distribution of contact normals. Computing void vectors or particle orientations is relatively more complicated as they require special algorithms or non-spherical particles. Fu & Dafalias (2011) and Wang et al. (2017) found that a unique state is reached for each of these fabric definitions after sufficient shearing, irrespective of the initial void ratio and the initial fabric anisotropy of the specimen. Therefore, in this study, we limit our focus on contact-based fabric tensors. The methodology developed in this study, however, is general and can be readily applied to other types of fabric tensors.

It is possible to identify three kinds of fabric tensors given a set of directional data. Consider the following directional distribution of the total- and the strong-contact normals:

$$\rho(\mathbf{n}) = \frac{2N_c}{N_p}\bar{\rho}_c(\mathbf{n}) = \Delta\bar{\rho}_c(\mathbf{n}); \quad \rho^s(\mathbf{n}) = \frac{2N_c^s}{N_p}\bar{\rho}_c^s(\mathbf{n}) = \Delta^s\bar{\rho}_c^s(\mathbf{n}) \tag{1}$$

where N_c is the number of contacts; N_p the number of particles in the assembly; $\bar{\rho}_c(\mathbf{n})$ the directional distribution density of contacts normals; **n** is the unit normal vector that spans over all directions; N_c^s is the number of strong contacts; $\bar{\rho}_c^s(\mathbf{n})$ is the directional distribution density of strong-contact normals. The strong contact is a subset of the overall contact and is defined here as the contact that transmit a normal force f_n greater than the average normal force $\langle f_n \rangle$ of all contacts (Radjai, 1996). Throughout this paper, superscript "*s*" is used to denote quantities for the strong contact network as in Eq. (1).

By the definition of distribution density $\int_{4\pi} \bar{\rho}(\mathbf{n})d\Omega = 1$ where $\Omega \in [0, 4\pi]$ is the solid angle, it follows that $\Delta = \int_{4\pi} \rho(\mathbf{n})d\Omega = 2N_c / N_p$ represents the average contacts per particle (or the coordination number). The fabric tensor of the first kind can be defined as (Kanatani, 1984):

$$G_{ij} = \int_{4\pi} \rho(\mathbf{n}) n_i n_j d\Omega \tag{2}$$

where n_i with i = 1, 2, 3 is the component of the contact normal. It is straightforward to show that the trace of G_{ij} is exactly the coordination number, i.e. $G_{kk} = \Delta$. Alternatively, it is also possible to approximate Eq. (1) by a second-order tensor:

$$\rho(\mathbf{n}) \approx \frac{1}{4\pi} E_{ij} n_i n_j \tag{3}$$

where E_{ij} is the fabric tensor of the second kind (Kanatani, 1984). It can be shown that $\Delta = \frac{1}{3}E_{kk}$ by integrating Eq. (3) over all directions. Multiplying Eq. (3) with $n_k n_l$ and integrate over [0, 4π] gives the relation between E_{ij} and G_{ij}:

$$E_{ij} = \frac{15}{2}\left(G_{ij} - \frac{1}{5}\Delta\delta_{ij}\right) \tag{4}$$

The deviatoric part of E_{ij} can be expressed as:

$$F_{ij} = E_{ij} - \frac{1}{3}E_{kk}\delta_{ij} = \frac{15}{2}\left(G_{ij} - \frac{1}{3}\Delta\delta_{ij}\right) \tag{5}$$

which is called the fabric tensor of the third kind. Substituting Eq. (5) into (3) gives:

$$\rho(\mathbf{n}) \approx \frac{1}{4\pi}\left(\Delta + F_{ij}n_i n_j\right) \tag{6}$$

which can be viewed as the spherical harmonic expansion of $\rho(\mathbf{n})$ truncated to the second order (Kanatani, 1984). It should be noted that all three fabric tensors have been used to approximate the directional statistics in the granular mechanics literatures. The advantage of G_{ij} is that it can be easily computed when then the directional distribution $\rho(\mathbf{n})$ is known (via Eq. (2)); E_{ij} is convenient when the goal is to map the fabric tensor back to a distribution (via Eq. (3)); F_{ij} is the deviatoric part of E_{ij} which is a zero-trace tensor. The three fabric tensors are interrelated through Eqs. (4) and (5), thus they are equivalent in representing soil microstructures. In practice, G_{ij} (and hence E_{ij}, F_{ij}) can be estimated from the discrete data of contact normals by:

$$G_{ij} = \frac{2}{N_p}\sum_{c\in C} n_i^c n_j^c \tag{7}$$

where the summation c is performed over all contacts C. The normalized fabric tensors can be correspondingly defined as:

$$\bar{G}_{ij} = G_{ij}/\Delta;\ \ \bar{E}_{ij} = E_{ij}/\Delta;\ \ \bar{F}_{ij} = F_{ij}/\Delta \tag{8}$$

Note that many DEM studies have reported their fabric data in terms of normalised fabric tensors (e.g. Thornton & Zhang, 2010; Yimisiri & Soga, 2010; Zhao & Guo, 2013; Yang & Wu, 2016; Zhou et al., 2017; Shi & Guo, 2018; Wang et al., 2019) which correspond to $\bar{G}_{ij}$, $\bar{E}_{ij}$ and $\bar{F}_{ij}$ in this study. Following the same mathematics Eqs. (2)-(8), one can define the fabric tensors corresponding to strong contact network: G_{ij}^s, E_{ij}^s and F_{ij}^s. The strong-contact coordination number $\Delta^s = \int_{4\pi} \rho^s(\mathbf{n})d\Omega = 2N_c^s / N_p = \frac{1}{3}E_{kk}^s = G_{kk}^s$ characterises the average number of strong contacts per particle.

STRESS-STRAIN-FABRIC DATA FROM TRUE TRIAXIAL TESTS

Drained behaviour

A total of 40 CID simulations were performed for isotropically consolidated specimens with p = 50 ~ 2000 kPa and b = 0 ~ 1 as shown in Table 2. The deviatoric part of F_{ij} and $\bar{F}_{ij}$ is selected to represent the degree of fabric anisotropy of the granular assembly:

$$F = \sqrt{\frac{3}{2} F_{ij} F_{ij}}; \quad \bar{F} = \sqrt{\frac{3}{2} \bar{F}_{ij} \bar{F}_{ij}} = \sqrt{\frac{3}{2} F_{ij} F_{ij}} \Big/ \Delta = F/\Delta \tag{9}$$

The stress strain behaviour and evolution of fabric anisotropy of CID tests are examined, and the results of triaxial compression (b = 0) and extension (b = 1) are presented in Fig. 2. It shows that the deviatoric stress ratio $\eta = q/p$ and normalized fabric anisotropy F/Δ of the simulations have reached the steady state around ε_a = 20 ~ 30%. The critical state η is 0.77 for compression tests and is 0.61 for extension tests. It is also observed that both deviatoric stress and fabric anisotropy in triaxial extension test evolves faster than that in triaxial compression tests. This phenomenon is similarly found in previous DEM studies (Huang et al., 2014; Zhou et al., 2017), which still lack a mechanistic explanation. In both types of test, F/Δ at critical state decreases with the increase of p, which is consistent with the observation by Zhao & Guo (2013).

As discussed in the introduction, useful information about granular packing is lost if one just looks at the normalised fabric tensor $\bar{F}$. Here we interpret the critical fabric data via the fabric tensor of the second kind E_{ij} whose trace is 3Δ and deviator is F_{ij}. Fig. 2 visualizes the principal values of E_{ij} and E_{ij}^s at critical state of all the CID tests. These data are determined by averaging the principal fabric values in the range of ε_a = 40% ~ 50% with the consideration that critical state is well reached after ε_a = 40% (as shown in Fig. 2) in order to minimize the effect of data oscillation in DEM simulations. Fig. 3 shows the critical fabric of CID test in principle fabric space (i.e. E_1-E_2-E_3 space). It is observed that tests conducted at higher pressure levels have larger CN for both total and strong contact networks. The size of the total-contact CFS is relatively constant with respect to the hydrostatic axis while the

strong-contact CFS significantly expands with the increase of Δ^s. Fig. 4 plots the values of Δ and Δ^s at critical state under various p, showing that their variations are negligible regardless of the loading path. This confirms that each critical fabric envelop in Fig. 3 is approximately on the same π-plane.

The shape of CFS in the π-plane can be described as follows (Zhang et al., 2020):

$$F(\theta) = F^{b=0} g(\theta) \tag{10}$$

where $\sqrt{2/3}F$ is the distance from the fabric state to the hydrostatic line (i.e. $E_1 = E_2 = E_3$) in the fabric space; superscript b=0 denotes the b value that the quantity is evaluated at; $g(\theta)$ is an interpolation function with respect to the Lode angle θ taken from Li & Dafalias (2004):

$$g(\theta) = \frac{\sqrt{(1+c^2)^2 + 4c\left(1-c^2\right)\sin 3\theta} - \left(1+c^2\right)}{2\left(1-c\right)\sin 3\theta} \tag{11}$$

where c is a material parameter. $g(\theta)$ varies smoothly from 1 for triaxial compression ($\theta = -30^\circ$) to c for triaxial extension ($\theta = 30^\circ$). c controls the shape of the CFS in the fabric π-plane and can be calculated by $c = F^{b=1}/F^{b=0}$ where the superscript denotes the shear mode the fabric tensor corresponds to.

Fig. 5(a) shows the total-contact CFS in the regular and normalised fabric π-plane. The critical fabric envelopes are best fitted by Eqs. (10) and (11) shown in the left figure. It is observed that the critical values of $F^{b=0}$ under different pressure levels are almost the same, while the shape of CFS slightly varies from circle to triangular with increasing p. The right figure shows the same envelops each normalised by the corresponding average critical CN of different b values (Δ_{ave}). It shows that the lower p leads to larger and more rounded normalized CFS, consistent with the observation by Zhao & Guo (2013). The critical fabric envelops for strong contacts are shown in Fig. 5(b) and are also fitted by Eq. (11) with different c. Unlike the total-contact CFS, the envelops for strong contacts enlarge with the increases of p without much change on the shape (i.e. c = 0.83~0.87). On the normalised fabric π-plane, all strong-contact envelops collapse into a single curve, indicating a linear relation between F_{ij}^s and Δ^s at critical state. The critical stress envelops from CID tests and

256 the fitted surfaces by Eq. (11) are shown in Fig. 5(c). Similar to the strong-contact CFS,
257 normalization of the stress envelopes with p produces a single critical-state stress ratio
258 surface.

259 The similarity between Fig. 5(c) and Fig. 5(b) has been also observed earlier in the
260 studies by Thornton & Zhang (2010) and Shi & Guo (2018). This leads to the proposal of a
261 linear, Lode-angle independent relationship between the strong-contact fabric ratio and the
262 stress ratio q/p by Shi & Guo (2018). The results here, however, highlights a minor difference
263 between the two: the shape of critical-state stress surface is slightly more trigonal than the
264 shape of the strong-contact CFS. This is quantified by the average shape parameter c = 0.79
265 of the former, which is 0.92 times of the latter with average c = 0.86. It can be inferred that
266 the slope of the strong-contact fabric evolution curve in triaxial compression should be 0.92
267 times of that in triaxial extension. This point will be further discussed in the *Fabric Evolution*
268 Section.

269 ***Undrained behaviour***

270 So far, the critical fabric surfaces for total- and strong-contact fabric tensors are
271 constructed based on the data from CID tests only. A set of undrained tests is desirable for the
272 following reasons: 1) it is not known whether the CFS in Fig. 3 is unique and independent of
273 drainage conditions, and 2) only a portion of CFS with limited range of coordination number
274 could be accessed by CID tests, i.e. 3.29 ~ 5.31 for the total-contact fabric and 1.26 ~ 2.05 for
275 the strong-contact fabric as shown in Fig. 4. CIU test permits the liquefaction of the specimen
276 and thus the access of critical fabric data in the low CN regime. The stress-strain curves and
277 stress paths of CIU triaxial compression ($b_e = b = 0$) and extension ($b_e = b = 1$) tests are
278 shown in Fig. 6. The slopes of the CSL in p-q space for compression and extension tests are
279 M_c = 0.77 and M_e = 0.61, respectively. The value of c for the critical stress surface is hence
280 obtained as $c = M_c/M_e$ = 0.792, which is consistent with the CID test results (Fig. 5(c)).

281 Fig. 7(a) and (b) presents respectively the total and strong-contact fabric path on the $\Delta - F$
282 plane under CIU triaxial conditions. For all tests, it is observed that the initial Δ increases
283 with respect to increasing consolidation pressure p_0. At the beginning of the shearing, F

rapidly increases while Δ decreases slightly. As loading continues, several tests under small initial confining pressures are liquefied, marked by the fact that Δ and F quickly evolves to zero as indicated by the dash lines in Fig. 7. After initial liquefaction, as the axial strain keeps increasing, the fabric states of liquified samples start to evolve following a unique curve which is independent of the initial conditions of the specimen and finally reach a steady state somewhere along this curve. This post-liquefaction fabric curve spans between Δ = 0-2.5 for total contacts and Δ^s = 0-1 for strong contacts. At the same time, the stresses of these specimens still remain almost zero even the fabric states are evolving in this post-liquified regime. This finding is consistent with the observation by Wang et al. (2016, 2019) that the fabric anisotropy only varies within a limited range after p reaches zero in cyclic tests. If the liquified state is considered as a critical state, the fabric path drawn by the liquified specimens can be considered as the continuation of the CFS established in the CID tests, providing the full geometry of the CFS in both pre- and post- liquefaction regime. For non-liquefied CIU tests, F first increases to the peak value then drops slightly and become stable at the critical state. The terminal values of Δ is consistently higher for higher p_0 specimens regardless of whether they are liquified or not. These critical fabric states will be plotted together with the CID data in the next section to check if the CFS is unique and independent of the drainage condition.

CRITICAL STATE LINE AND CRITICAL FABRIC SURFACE

Critical state line in the e-p and Δ-p space

From the above simulations, we have extracted the critical states of the following quantities: e, q, p, F, F^s, Δ and Δ^s. The conventional CSL in the e-p plane is plotted in Fig. 8(a). The data can be well represented by the power-law function of Li & Wang (1998), $e = 0.625 - 0.0022\left(p/p_a\right)^{1.36}$, where p_a is the atmosphere pressure. Fig. 8(b) shows that the critical values of Δ and p also collapse into a single line in the Δ-p plane. Such line is independent of the drainage condition and the shearing mode (different b or b_e values), which can be represented by a power-law function $CN = 3.00 + 0.47\left(p/p_a\right)^{0.53}$ as well. This

observation is consistent with the DEM results by Nguyen et al. (2017, 2018).

Critical fabric surface

As shown previously, Eqs. (10) and (11) well capture the shape of critical state envelops obtained from CID tests. However, the critical fabric data from CIU tests does not locate on fixed fabric π-planes, making the calibration of the shape coefficient c difficult (assuming Eqs. (10) and (11) are still valid). An alternative approach is to calculate the value of c using its definition $c = F^{b=1}/F^{b=0}$, and then check if the plotted surface pass through all data points. Note from Fig. 7 that both $F^{b=1}$ and $F^{b=0}$ vary with respect to Δ, it is thus expected that c is a function of Δ as well, i.e. $c(\Delta) = F^{b=1}(\Delta)/F^{b=0}(\Delta)$. Therefore, our strategy here is to use Eqs. (10) and (11) combined with a $F^{b=0}(\Delta)$ and $c(\Delta)$ function to construct a 3D CFS in the principal fabric space, in hoping to represent the critical fabric data from both CID and CIU tests.

The critical values of $F(\Delta)$ and $F^s(\Delta)$ obtained from all true triaxial tests under b=0 and b=1 are summarized in Fig. 9(a) and 9(b), respectively. One can see that each curve is separated by a threshold Δ value (i.e., Δ_t or Δ_t^s) below which the critical fabric data comes from liquified samples and the rest from non-liquified samples. All curves pass through the origin, confirming that no fabric anisotropy could develop if no contact exists. Fig. 9(a) shows that the critical F-Δ envelope for the total-contact fabric is quite nonlinear. The following equation is selected to best fit this data:

$$y(x) = \frac{x}{a_1 + a_2\sqrt{x} + a_3 x} \tag{12}$$

where a_1, a_2, and a_3 are fitting parameters. This is the so-called Gunary equation which is firstly used by Gunary (1970) to describe the adsorption isotherm for phosphate in soils. The characteristics of Gunary equation is shown in Fig. 10. It starts at (0, 0), goes through (1, $1/(a_1+a_2+a_3)$) and converges to (∞, $1/a_3$). The slope at x = 1 is a constant and equals to $(a_1+0.5a_2)/(a_1+a_2+a_3)^2$. With three coefficients, the initial slope, the intermediate transition and the ultimate asymptotic of the curve can be controlled, providing the flexibility to capture

the present dataset. The coefficients used for fitting the F-Δ data are shown in Fig. 9(a). For strong-contact fabric, its F^s-Δ^s envelope is just slightly nonlinear and is conveniently fitted by a power-law equation as shown in Fig. 9(b). The shape coefficient c is obtained by taking the ratio between $F(\Delta)$ for b=1 and that for b=0, the same for c^s for the strong-contact fabric. The computed $c(\Delta)$ and $c^s(\Delta^s)$ curves are shown in Fig. 11. It shows that c decreases first and then increases with respect to Δ, implying that the shape of the cross sections of the total-contact CFS is constantly morphing. The $c^s(\Delta^s)$ curve, on the other hand, exhibits a gradual increasing trend.

The critical fabric surface can be finally plotted in the principal fabric space (i.e., E_1-E_2-E_3 space with $\Delta = E_{kk}/3$ and $F = \sqrt{3/2\, F_{ij}F_{ij}}$) by substituting the $F^{b=0}(\Delta)$ and $c(\Delta)$ relations into Eqs. (10) and (11), as shown in Fig. 12. It is observed that the shapes of the total- and the strong-contact CFSs are both cones with different rates of expansion along the hydrostatic axis. Recalling only CID and CIU (b_e = 0, 1) tests are used in the development of the CFS, the remaining data from CIU (b_e = 0.25, 0.5, 0.75), CID_e_0 and CK$_0$D tests (44 in total) can be used for blind evaluations of the uniqueness of the CFS. The deviation between the mathematical CFS and the critical fabric data from these tests is quantitatively assessed by calculating the R^2 value. The 44 critical fabric data points together with the constructed CFS are plotted in the left side of Fig. 13. One can qualitatively see that all the data for both liquefied and non-liquefied specimens fall on this mathematical CFS. For a specific critical fabric data (F_{data}, Δ_{data}, θ_{data}), its corresponding F on the CFS can be calculated by $F(\Delta_{data}$, $\theta_{data})$ using Eq. (10) and is denoted as F_{CFS}. The comparison of F_{data} and F_{CFS} is then shown in the right side of Fig. 13. The R^2 values are 0.9448 for the total-contact CFS and 0.9890 for the strong-contact CFS, which quantitatively validates the uniqueness of the CFS. It is noted that the strong-contact CFS has a better consistency overall than the total-contact CFS. This is partially due to the fact that the 3-parameter Gunary equation does not fit the total fabric $F^{b=0}(\Delta)$ data as good as that of the power-law equation for strong-fabric $F^{s,\,b=0}(\Delta^s)$ data, as shown in Fig. 9. Better capturing of the total-contact CFS, especially for improved performance at low Δ values, can be achieved by using more sophisticated fitting equations

such as a 5th order polynomial function. In conclusion, the DEM data supports the two key hypotheses of this study: 1) the CFS is unique, independent of the drainage condition and the initial state of the specimen; 2) the cross-sections of CFS in the liquefied regime (i.e. at low Δ values) can be satisfactorily captured by Eqs. (10) and (11). These conclusions are true for both the total- and the strong-contact fabric tensors as seen in Fig. 13(a) and (b), respectively.

The CFS provides an elegant and unified platform to synthesize many recent research results on granular soils. First, the cross sections of CFS perpendicular to the hydrostatic axis reflects the fabric anisotropy of a granular specimen develops at critical state as studied in several earlier works (Yimisiri & Soga, 2010; Thornton & Zhang, 2010; Zhao & Guo, 2013; Zhou et al., 2017; Shi & Guo, 2018). Second, cutting the CFS along the hydrostatic axis gives a F-Δ envelope that attracts the fabric paths during shearing, which is consistent with the critical-state *CN-A* relation discussed in Kruyt & Rothenburg (2014). Besides the above unifications, the CFS also compiles the critical fabric data for liquefied specimens, thus defining a single ultimate state for granular soils in both pre- and post- liquefaction regimes. Finally, the concept of CFS may help unify the various CSLs observed in the *e-p-q* or the *A-e-p-q* space. Zhang et al. (2020) has recently made a theoretical attempt exploring such direction and showed that a simple constitutive model based on CFS can reproduce many characteristic behaviours of granular soils including the classical asymptotic states of CST and ACST. In summary, much essential information about soil fabric at critical state can be extracted from the proposed CFS, simplifying the data presentation, and offering new insights for theoretical developments.

FABRIC EVOLUTION

The CFS describes the ultimate state of fabric tensor after sufficient shearing but does not tell the path towards such state. This section investigates the evolution of fabric tensor by looking at the fabric ratio $\bar{F} = F / \Delta$ versus the stress ratio $\eta = q / p$ data obtained from the CID, CIU and CK_0D tests.

Fig. 14 presents the fabric evolution curves of CID test under different b and p values.

Fig. 14(a) implies that that $\bar{F}$ has a monotonically increasing relationship with η. Right before reaching the critical state, both $\bar{F}$ and η reduces proportionally and then become steady at critical state while the shear strain continuous. Such curve however is highly nonlinear, pressure-dependent and Lode-angle dependent for the total-contact fabric. Modelling of such curve requires incremental relations that are quite *ad-hoc* (Yuan et al. 2019). On the contrary, the strong-contact fabric exhibits a much straightforward $\bar{F}^s - \eta$ relation as shown in Fig. 14(b). Specifically, all data regardless of the pressure level and the shearing mode can be approximated by a single line with a slope of 2.14. The above results have been similarly observed by Shi & Guo (2018) who reported a slope of $G_q^s / G_p^s = 0.9q/p$, where G_q^s is the deviatoric part of G_{ij}^s. Taking advantage of Eq. (5), $G_q^s / G_p^s = 0.9q/p$ can be converted to $\bar{F}^s = 2.25\eta$ which has a slightly higher slope than the one obtained in this study. Another observation is that the best-fit slopes for only the b=1 and the b=0 data are 2.235 and 2.056, respectively. The slope of the data under b=0 is exactly 0.92 times that under b=1, leading to the average c value of critical state stress surface (i.e. 0.79) becomes 0.92 times the average c value of strong-contact CFS (i.e. 0.86), as commented in the *Drained Behaviour* subsection. This reveals that the $\bar{F}^s - \eta$ relation is not strictly Lode-angle independent as discussed in Shi & Guo (2018).

The fabric evolution of CIU test is shown in Fig. 15. Observation of Fig. 15(a) reveals that the $\bar{F} - \eta$ curves for non-liquefied samples share similar trend of those from CID tests. For liquified samples, some remarkable features are observed: 1) at the beginning of shearing, $\bar{F}$ gradually increase with η but soon become scattered once the specimen is liquefied; 2) the scattered data tends to concentrate on a few narrow regions for all shearing modes as shearing continues. Fig. 15(b) shows that the strong-contact fabric again obeys a linear fabric evolution with respect to η with the same slope 2.14 obtained from the CID tests, although with some scatters. It is worth to note that little attention has been paid in classical soil mechanics research to the properties of post-liquefied sand including its internal structure. The present result shows that the soil's microstructure may still maintain some relations at a

stress state near the limit of p=q=0. Such fabric-stress relation may be conducive for studies on cyclic liquefaction of sand and dense granular flow problems.

Fig. 16 plots the fabric evolutions of CK_0D test compared with those from the previous CID test. The initial state is reached by anisotropically consolidating the specimen to p=1000 kPa with b = 0 under pre-set K_0 values (0.625 or 0.75). The initial conditions for the K_0 = 0.75 and K_0 = 0.625 tests are ($\eta_0 = 0.3$, $\bar{F}_0 = 0.097$, $\bar{F}_0^s = 0.662$) and ($\eta_0 = 0.5$, $\bar{F}_0 = 0.198$, $\bar{F}_0^s = 1.072$), respectively. Shearing is then performed following different b paths. Fig. 16(a) shows that the fabric evolution starts at a point off the CID curves, implying that the evolution of $\bar{F}$ is stress-history dependent. Then the $\bar{F} - \eta$ data deviates significantly from the CID curves before it converges to the same critical state position for sample that is sheared under the same mode. Observation of Fig. 16(b) shows that all the strong-contact data including the initial state are located on the previously identified $\bar{F}^s - \eta$ line with a slope of 2.14. This confirms that this line is not affected by the consolidation method and is independent of the stress history. In summary, the evolution of strong-contact fabric evolution is hardly affected by the consolidation condition, while the evolution of total-contact fabric is more complicated and needs further investigations.

CONCLUSIONS

This study explores the characteristics of fabric anisotropy of granular soils at critical state through 100 true triaxial DEM simulations. Among them, 56 critical-state fabric data points are used identify a critical fabric surface that attracts the fabric state of granular specimens upon shearing. The rest 44 data points are used to validate the uniqueness of such surface for samples prepared and sheared at different conditions. The evolution of fabric path towards the CFS is also investigated. The main conclusions of this study are highlighted below:

(1) A granular assembly has a unique critical fabric surface (for the given fabric tensor definition) that is independent of the shearing mode, the initial state of the specimen

445 and the drainage condition.

446 (2) The CFS spans across a wide range of coordination numbers, including the
447 apparently liquefied regime. This means that fabric states maintain some geometrical
448 relations even if the effective stress is approximately zero.

449 (3) The evolution of the strong-contact fabric tensor with respect to stress ratio is linear
450 and is independent of the shear mode and pressure level. This relation also works for
451 the liquefied specimens and is not affected by the consolidation method. The
452 evolution of total-contact fabric is not as straightforward but depends on the stress
453 level, shear mode and stress history.

454 The CFS synthesizes the rich information about the soil microstructure developed at
455 critical state and provides new perspectives in interpreting the critical state phenomenon. This
456 concept may be useful in the constitutive modelling of granular soils and in understanding the
457 micromechanics of sand liquefaction, as demonstrated in the recently proposed critical fabric
458 theory (Zhang et al., 2020).

459 It is worth mentioning that in Zhang et al. (2020), the strong-contact fabric rather than
460 the total-contact fabric is utilized for model development because of the simple linear relation
461 between the strong-contact fabric and stress. The present paper further shows that the
462 geometry of the total-contact CFS is also more complex than that of the strong-contact CFS
463 or critical state stress surface. For these reasons, it may seem that strong-contact fabric is
464 more useful than total-contact fabric in modelling granular soils. However, obtaining the
465 statistics of strong contacts require information about the force chain network which is
466 difficult to measure experimentally.

467 The present study uses conventional DEM simulation to locate the CFS of a granular
468 assembly. One limitation of this approach is the highly idealized particle shape. Some recent
469 DEM-based schemes (Kawamoto et al., 2016; Nadimi & Fonseca, 2018; Zhang et al., 2018)
470 present alternative approaches for a more accurate representation of particle shapes and
471 contact topologies found in real sands. In addition, further studies are needed to deepen our
472 understanding on the evolution of fabric towards the CFS especially during cyclic loading

paths. The relations between fabric and other state descriptors as void ratio or porosity are still unclear and require systematic studies.

ACKNOWLEGEMENT

Yida Zhang wishes to express thanks for the start-up fund provided by the Department of Civil, Environmental and Architectural Engineering at the University of Colorado Boulder. The assistances on YADE by Mingdong Jiang, Yihong Xie and Prof. Zhongxuan Yang from Zhejiang University is highly appreciated.

REFERENCES

Cundall, P. A., & Strack, O. D. L. (1979). A discrete numerical model for granular assemblies. *Géotechnique*, **29**, No. 1, 47-65, https://doi.org/10.1680/geot.1979.29.1.47.

da Cruz, F., Emam, S., Prochnow, M., Roux, J. N., & Chevoir, F. (2005). Rheophysics of dense granular materials: Discrete simulation of plane shear flows. *Phys. Rev. E* **72**, No. 2, 021309.

Dafalias, Y. F., & Taiebat, M. (2016). SANISAND-Z: zero elastic range sand plasticity model. *Géotechnique*, **66**, No. 12, 999-1013, https://doi.org/10.1680/jgeot.15.P.271.

Fonseca, J., O'sullivan, C., COOP, M. R., & Lee, P. D. (2013a). Quantifying the evolution of soil fabric during shearing using directional parameters. *Géotechnique*, **63, No.** 6, 487-499.

Fonseca, J., O'sullivan, C., Coop, M. R., & Lee, P. D. (2013b). Quantifying the evolution of soil fabric during shearing using scalar parameters. *Géotechnique*, **63**, No. 10, 818-829.

Fu, P., & Dafalias, Y. F. (2011). Fabric evolution within shear bands of granular materials and its relation to critical state theory. *Int. J. Numer. Anal. Meth. Geomech.* **35**, No. 18, 1918-1948.

Fu, P., & Dafalias, Y. F. (2015). Relationship between void-and contact normal-based fabric tensors for 2D idealized granular materials. *Int. J. Solids Struct.* **63**, 68-81.

Gu, X., Huang, M., & Qian, J. (2014). DEM investigation on the evolution of microstructure in granular soils under shearing. *Granul. Matter* **16**, No. 1, 91-106.

500 Gunary, D. (1970). A new adsorption isotherm for phosphate in soil. *J. Soil Sci.* **21**, No. 1,
501 72-77.
502 Guo, N., & Zhao, J. (2013). The signature of shear-induced anisotropy in granular
503 media. *Comput. Geotech.* **47**, 1-15.
504 Guo, N., & Zhao, J. (2014). Local fluctuations and spatial correlations in granular flows
505 under constant-volume quasistatic shear. *Phys. Rev. E* **89**, No. 4, 042208.
506 Gao, Z., & Zhao, J. (2017). A non-coaxial critical-state model for sand accounting for fabric
507 anisotropy and fabric evolution. *Int. J. Solids Struct.*, **106**, 200-212.
508 Huang, X., Hanley, K. J., O'Sullivan, C., Kwok, C. Y., & Wadee, M. A. (2014). DEM
509 analysis of the influence of the intermediate stress ratio on the critical-state behaviour of
510 granular materials. *Granul. Matter,* **16**, No. 5, 641-655.
511 Imseeh, W. H., Druckrey, A. M., and Alshibli, K. A. (2018). 3D experimental quantification
512 of fabric and fabric evolution of sheared granular materials using synchrotron
513 micro-computed tomography. *Granul. Matter* **20**, No. 2, 24.
514 Kawamoto, R., Andò, E., Viggiani, G. and Andrade, J.E., 2016. Level set discrete element
515 method for three-dimensional computations with triaxial case study. *J. Mech. Phys.*
516 *Solids* **91**, 1-13.
517 Kruyt, N. P., & Rothenburg, L. (2014). On micromechanical characteristics of the critical
518 state of two-dimensional granular materials. *Acta Mech*. **225**, No. 8, 2301-2318.
519 Kruyt, N. P., & Rothenburg, L. (2016). A micromechanical study of dilatancy of granular
520 materials. *J. Mech. Phys. Solids.* **95**, 411-427.
521 Kuhn, M. R. (2010). Micro-mechanics of fabric and failure in granular materials. *Mech.*
522 *Mater.*, **42**, No. 9, 827-840.
523 Kuhn, M. R., Sun, W., & Wang, Q. (2015). Stress-induced anisotropy in granular materials:
524 fabric, stiffness, and permeability. *Acta Geotech.,* **10**, No. 4, 399-419.
525 Li, X. S., & Dafalias, Y. F. (2004). A constitutive framework for anisotropic sand including
526 non-proportional loading. *Géotechnique* **54**, No. 1, 41-55,
527 https://doi.org/10.1680/geot.2004.54.1.41.

528 Li, X. S. & Dafalias, Y. F. (2012). Anisotropic critical state theory: role of fabric. *J. Engng*
529 *Mech. ASCE* **138**, No. 3, 263-275.
530 Li, X. S., & Dafalias, Y. F. (2015). Dissipation consistent fabric tensor definition from DEM
531 to continuum for granular media. *J. Mech. Phys. Solids* **78**, 141-153.
532 Li, X. S., & Wang, Y. (1998). Linear representation of steady-state line for sand. *J. Geotech.*
533 *Geoenviron. Engng*, **124**, No. 12, 1215-1217.
534 Lopera Perez, J. C., Kwok, C. Y., O'Sullivan, C., Huang, X., & Hanley, K. J. (2016).
535 Assessing the quasi-static conditions for shearing in granular media within the critical
536 state soil mechanics framework. *Soils Found.* **56**, No. 1, 152-159.
537 MiDi, G. D. R. (2004). On dense granular flows. *Eur. Phys. J. E.* **14**, No. 4, 341-365.
538 Nakata, Y., Hyodo, M., Murata, H. & Yasufuku, N. (1998). Flow deformation of sands
539 subjected to principal stress rotation. *Soils Found*. **38**, No. 2, 115–128.
540 Nadimi, S., & Fonseca, J. (2018). A micro finite-element model for soil behaviour.
541 *Géotechnique* **68**, No. 4, 290-302, https://doi.org/10.1680/jgeot.16.P.147.
542 Ng, T. T. (2006). Input parameters of discrete element methods. *J. Engng Mech. ASCE* **132**,
543 No. 7, 723-729.
544 Nguyen, H. B. K., Rahman, M. M., & Fourie, A. B. (2017). Undrained behaviour of granular
545 material and the role of fabric in isotropic and K_0 consolidations: DEM
546 approach. *Géotechnique* **67**, No. 2, 153-167, https://doi.org/10.1680/jgeot.15.P.234.
547 Nguyen, H. B. K., Rahman, M. M., & Fourie, A. B. (2018). Characteristic behavior of
548 drained and undrained triaxial compression tests: DEM study. *J. Geotech. Geoenviron.*
549 *Engng ASCE* **144**, No. 9, 04018060.
550 Radjai, F., Jean, M., Moreau, J. J., & Roux, S. (1996). Force distributions in dense
551 two-dimensional granular systems. *Phys. Rev. Lett.* **77**, No. 2, 274-277.
552 Roscoe, K. H., Schofield, A. N., & Wroth, C. P. (1958). On the yielding of soils.
553 *Géotechnique* **8**, No. 1, 22-53, https://doi.org/10.1680/geot.1958.8.1.22.
554 Salvatore, E., Modoni, G., Andò, E., Albano, M., & Viggiani, G. (2017). Determination of the
555 critical state of granular materials with triaxial tests. *Soils Found.,* **57**, No. 5, 733-744.

556 Schofield, A. N. & Wroth, C. P. (1968). Critical state soil mechanics. London, UK:
557 McGraw-Hill.
558 Shi, J., & Guo, P. (2018). Fabric evolution of granular materials along imposed stress
559 paths. *Acta Geotech.* **13**, No. 6, 1341-1354.
560 Thornton, C., & Antony, S. J. (2000). Quasi-static shear deformation of a soft particle
561 system. *Powder technol.* **109**, No.1-3, 179-191.
562 Thornton, C., & Zhang, L. (2010). On the evolution of stress and microstructure during
563 general 3D deviatoric straining of granular media. *Géotechnique* **60**, No. 5, 333-341,
564 https://doi.org/10.1680/geot.2010.60.5.333.
565 Wang, G., & Wei, J. (2016). Microstructure evolution of granular soils in cyclic mobility and
566 post-liquefaction process. *Granul. Matter* **18**, 51.
567 Wang, R., Fu, P., Zhang, J. M., & Dafalias, Y. F. (2016). DEM study of fabric features
568 governing undrained post-liquefaction shear deformation of sand. *Acta Geotech.* **11**, No. 6,
569 1321-1337.
570 Wang, R., Fu, P., Zhang, J. M., & Dafalias, Y. F. (2017). Evolution of various fabric tensors
571 for granular media toward the critical state. *J. Engng Mech. ASCE* **143**, No. 10,
572 04017117.
573 Wang, R., Fu, P., Zhang, J. M., & Dafalias, Y. F. (2019). Fabric characteristics and processes
574 influencing the liquefaction and re-liquefaction of sand. *Soil Dyn. Earthq. Engng* **125**,
575 105720.
576 Wiebicke, M., Andò, E., Salvatore, E., Viggiani, G., & Herle, I. (2017) "Experimental
577 measurement of granular fabric and its evolution under shearing." *Proc., EPJ Web of Conf.*
578 *EDP Sciences*, 02020.
579 Wiebicke, M., Andò, E., Viggiani, G. and Herle, I., (2020). Measuring the evolution of
580 contact fabric in shear bands with X-ray tomography. *Acta Geotech.* **15**, No. 1, pp.79-93.
581 Woo, S. I., & Salgado, R. (2015). Bounding surface modeling of sand with consideration of
582 fabric and its evolution during monotonic shearing. *Int. J. Solids Struct.* **63**, 277-288.
583 Xie, Y. H., Yang, Z. X., Barreto, D., & Jiang, M. D. (2017). The influence of particle

584 geometry and the intermediate stress ratio on the shear behaviour of granular
585 materials. *Granul. Matter* **19**, 35.
586 Yan, W. M., & Zhang, L. (2013). Fabric and the critical state of idealized granular
587 assemblages subject to biaxial shear. *Comput. Geotech.* **49**, 43-52.
588 Yang, Z. X., & Wu, Y. (2017). Critical state for anisotropic granular materials: a discrete
589 element perspective. *I. J. Geomech. ASCE* **17**, No. 2, 04016054.
590 Yimsiri, S., & Soga, K. (2010). DEM analysis of soil fabric effects on behaviour of
591 sand. *Géotechnique* **60**, No. 6, 483-495, https://doi.org/10.1680/geot.2010.60.6.483.
592 Yoshimine, M., Ishihara, K. & Vargas, W. (1998). Effects of principal stress direction and
593 intermediate principal stress on undrained shear behaviour of sand. *Soils Found*. **38**, No. 3,
594 179– 188.
595 Yuan, R., Yu, H. S., Yang, D. S., & Hu, N. (2019). On a fabric evolution law incorporating the
596 effects of b-value. *Comput. Geotech.* **105**, 142-154.
597 Zhang, B., Regueiro, R., Druckrey, A. and Alshibli, K., 2018. Construction of poly-ellipsoidal
598 grain shapes from SMT imaging on sand, and the development of a new DEM contact
599 detection algorithm. *Engng Comput*. **35**, No. 2, 733-771
600 Zhang, Y., Zhou, X., & Wen, Y. (2020). A constitutive theory for sand based on the concept of
601 critical fabric surface. *J. Engng Mech. ASCE* **146**, No. 4, 04020019.
602 Zhao, J., & Guo, N. (2013). Unique critical state characteristics in granular media considering
603 fabric anisotropy. *Géotechnique* **63**, No. 8, 695-704,
604 https://doi.org/10.1680/geot.12.P.040.
605 Zhou, W., Liu, J., Ma, G., & Chang, X. (2017). Three-dimensional DEM investigation of
606 critical state and dilatancy behaviours of granular materials. *Acta Geotech.* **12**, No. 3,
607 527-540.

NOTATION

a_1, a_2, a_3	parameters in the Gunary equation
b, b_e	principal stress ratio and principal strain ratio
c, c^s	shape parameter of the total- and strong- contact critical fabric surface
$d, \bar{d}$	particle diameter and average particle diameter
e	void ratio
E	particle Young's modulus
E_1, E_2, E_3	major, intermediate, and minor principal values of E_{ij}
E_1^s, E_2^s, E_3^s	major, intermediate, and minor principal values of E_{ij}^s
E_{ij}, E_{ij}^s	total- and strong-contact fabric tensor of the second kind
$\bar{E}_{ij}, \bar{E}_{ij}^s$	normalized total- and strong-contact fabric tensor of the second kind
F, F^s	deviatoric part of F_{ij} and F_{ij}^s
F_{data}, F_{data}^s	values of F and F^s from DEM data
F_{CFS}, F_{CFS}^s	projected values of F and F^s on the critical fabric surface using Δ_{data} and θ_{data}
F_n, F_s	normal and tangential forces at particle contact
$\bar{F}, \bar{F}^s$	deviatoric part of $\bar{F}_{ij}$ and $\bar{F}_{ij}^s$
$\bar{F}_0, \bar{F}_0^s$	initial values of $\bar{F}$ and $\bar{F}^s$
F_1, F_2, F_3	major, intermediate, and minor principal values of F_{ij}
F_{ij}, F_{ij}^s	total- and strong-contact fabric tensor of the third kind
$\bar{F}_{ij}, \bar{F}_{ij}^s$	normalized total- and strong-contact fabric tensor of the third kind
g, g^s	interpolation function that controls the shape of the total- and strong-contact critical fabric surface on the π-plane
G_p^s, G_q^s	mean and deviatoric part of the strong-contact fabric tensor of the first kind
G_{ij}, G_{ij}^s	total- and strong-contact fabric tensor of the first kind
$\bar{G}_{ij}, \bar{G}_{ij}^s$	normalized total- and strong-contact fabric tensor of the first kind
I	inertia number
k_n, k_s	normal and tangential stiffness of a particle
K_0	lateral stress ratio
K_n, K_s	normal and tangential stiffness of a contact
$\mathbf{n}$	contact normal vector
N_c, N_c^s	number of contacts and number of strong contacts
N_p	number of particles in the assembly
q	deviatoric stress
R	particle radius
p, p_0	mean effective stress and its initial value
δ_n, δ_s	normal and tangential displacement of a contact
δ_{ij}	Kronecker delta
Δ, Δ^s	total- and strong-contact coordination number
Δ_{data}	coordination number from DEM data

Δ_t, Δ_t^s	threshold coordination number of total- and strong-contact fabric
Δt_{cr}	critical time step
ε_1, ε_2, ε_3	major, intermediate, and minor principal strain
ε_a	axial strain
$\dot{\varepsilon}$	strain rate
η, η_0	stress ratio and its initial value
θ, θ^s	Lode angle in total- and strong-contact fabric space
θ_{data}	Lode angle from DEM data
μ	particle friction coefficient
ρ, ρ^s	directional distribution of total- and strong-contact normals
$\bar{\rho}_c, \bar{\rho}_c^s$	directional distribution density of total- and strong-contact normals
ρ_g	particle density
σ_1, σ_2, σ_3	major, intermediate, and minor principal effective stress
Ω	solid angle

LIST OF TABLES

Table 1. Initial void ratio of the specimens in CID and CIU tests

p (kPa)	50	100	300	500	700	1000	1500	2000
e_0	0.660	0.660	0.650	0.626	0.605	0.577	0.534	0.497

Table 2. DEM tests in this study

Test conditions	CID	CIU	CID_e_0	CK_0D
Mean normal stress p or p_0 (kPa)	p = 50, 100, 300, 500, 700, 1000, 1500, 2000	p_0 = 50, 100, 300, 500, 700, 1000, 1500, 2000	e_0 = 0.535, 0.590; p = 1000	K_0 = 0.625, 0.75; p = 1000
b (stress controlled) or b_e (strain controlled)	b = 0, 0.25, 0.5, 0.75, 1	b_e = 0, 0.25, 0.5, 0.75, 1	b = 0, 0.25, 0.5, 0.75, 1	b = 0, 0.25, 0.5, 0.75, 1
Number of tests	40	40	10	10

LIST OF CAPTIONS

Fig. 1. Grain size distribution of the DEM sample

Fig. 2. Stress-strain curve (left) and fabric evolution (right) in CID tests: (a) triaxial compression (b=0), (b) triaxial extension (b=1)

Fig. 3. Critical fabric data from CID tests with different confining pressures (p = 50 ~ 2000 kPa) and shearing modes (b = 0 ~ 1) in the principal fabric space: (a) total-contact fabric, (b) strong-contact fabric

Fig. 4. Critical-state coordination number (CN) from CID tests: (a) total-contact *CN*, (b) strong-contact *CN*

Fig. 5. Critical-state envelopes from CID test (left) and their normalised counterparts (right) in the π-plane: (a) total-contact fabric, (b) strong-contact fabric, (c) stress. Black solid lines are the best fit by Eqs. (10) and (11), with the values of c indicated in the legends

Fig. 6. Stress-strain curves (left) and stress paths (right) in CIU tests: (a) triaxial compression (b_e = 0), (b) triaxial extension (b_e = 1)

Fig. 7. Fabric paths in CIU triaxial compression (left) and extension (right) tests: (a) total-contact fabric, (b) strong-contact fabric

Fig. 8. Critical state lines on (a) the e-p plane and (b) the Δ-p plane

Fig. 9. Critical state F-Δ envelop in triaxial compression (left) and extension (right) tests: (a) total-contact fabric, (b) strong-contact fabric

Fig. 10. Characteristics of Gunary equation

Fig. 11. $\Delta - c$ relation of the total-contact and strong-contact CFS

Fig. 12. Critical fabric surface of (a) total-contact fabric and (b) strong-contact fabric

Fig. 13. Verification of the uniqueness of the critical fabric surface of (a) total-contact fabric and (b) strong-contact fabric using data from CIU, CID_e_0, and CK_0D tests. Figures on the left plot CFS and data in the principal fabric space. Figures on the right compare F data and F calculated by the CFS equation

Fig. 14. Fabric evolution of (a) total-contact fabric and (b) strong-contact fabric during CID tests under different values of b (left) and pressure (right)

Fig. 15. Fabric evolution of (a) total-contact fabric and (b) strong-contact fabric during CIU tests for non-liquefied (left) and liquified (right) samples

Fig. 16. Fabric evolution of (a) total-contact fabric and (b) strong-contact fabric during CK_0D tests with K_0 = 0.75 (left) and K_0 = 0.625 (right)

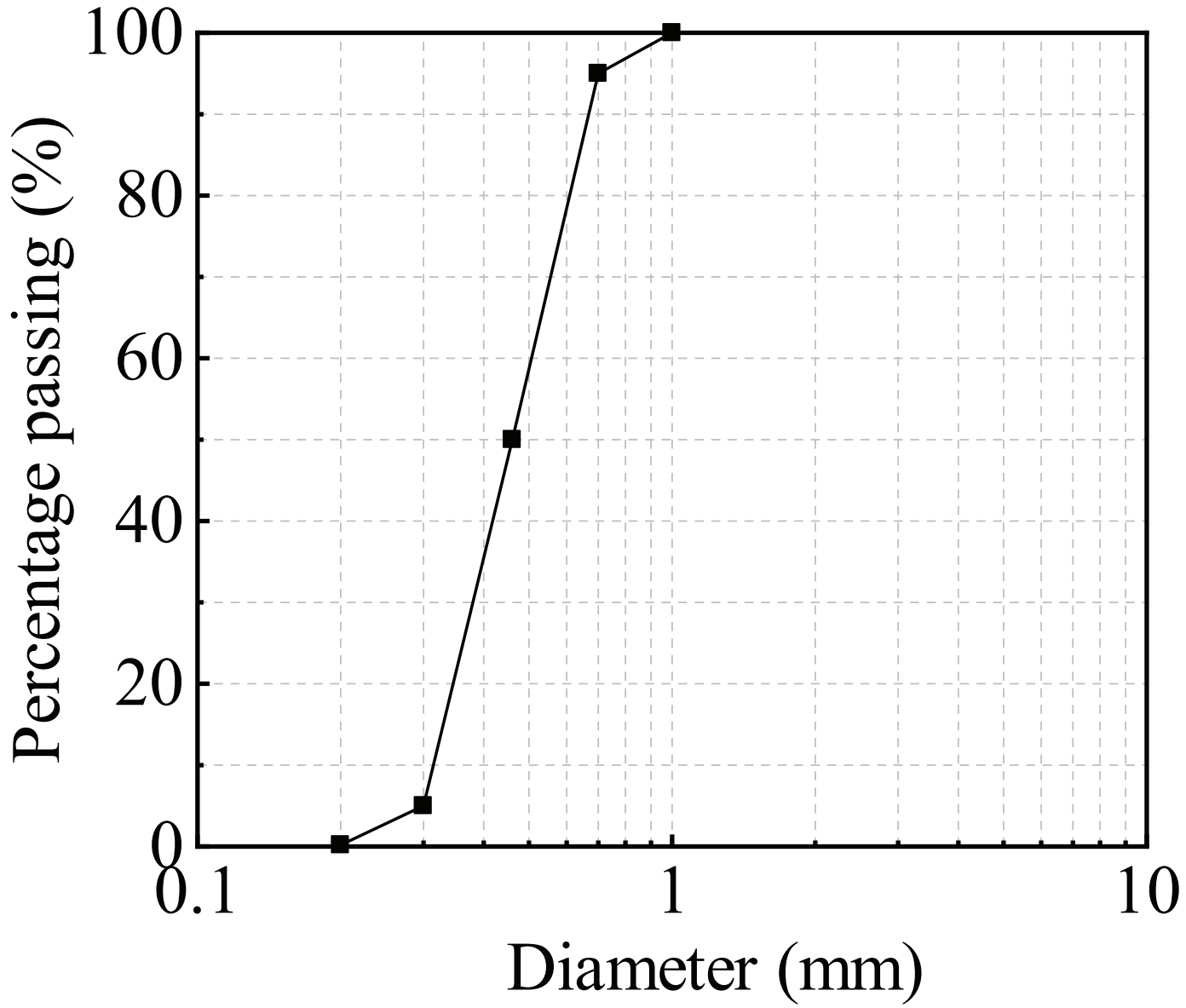
100
80
60
40
20
0
Percentage passing (%)
0.1
1
10
Diameter (mm)

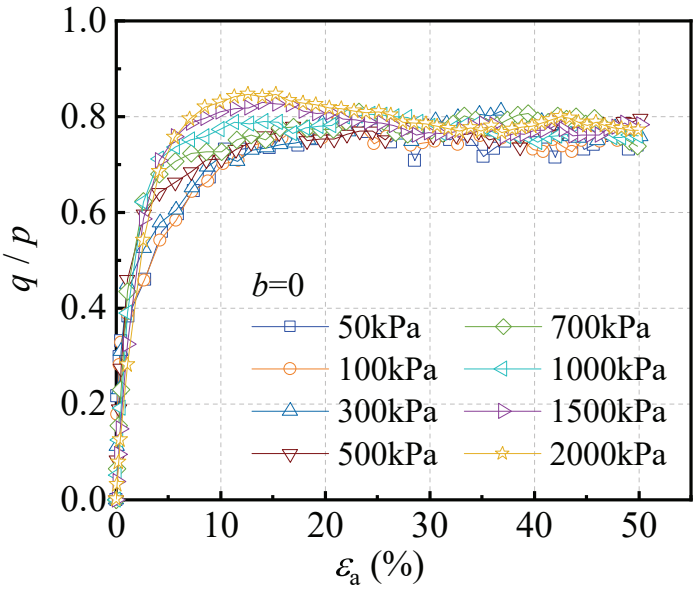
1.0
0.8
0.6
0.4
0.2
0.0
q / p
b=0
50kPa
100kPa
300kPa
500kPa
700kPa
1000kPa
1500kPa
2000kPa
0
10
20
30
40
50
εa (%)

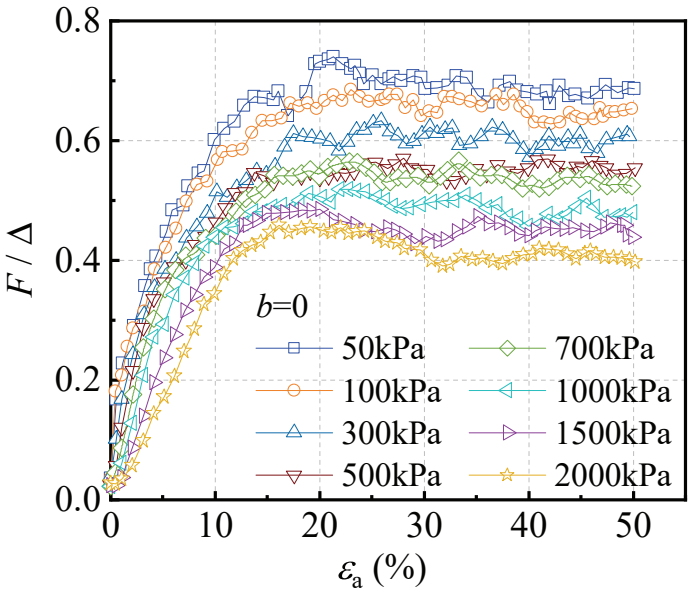
0.8
0.6
0.4
0.2
0.0
F / Δ
b=0
50kPa
100kPa
300kPa
500kPa
700kPa
1000kPa
1500kPa
2000kPa
0
10
20
30
40
50
εa (%)

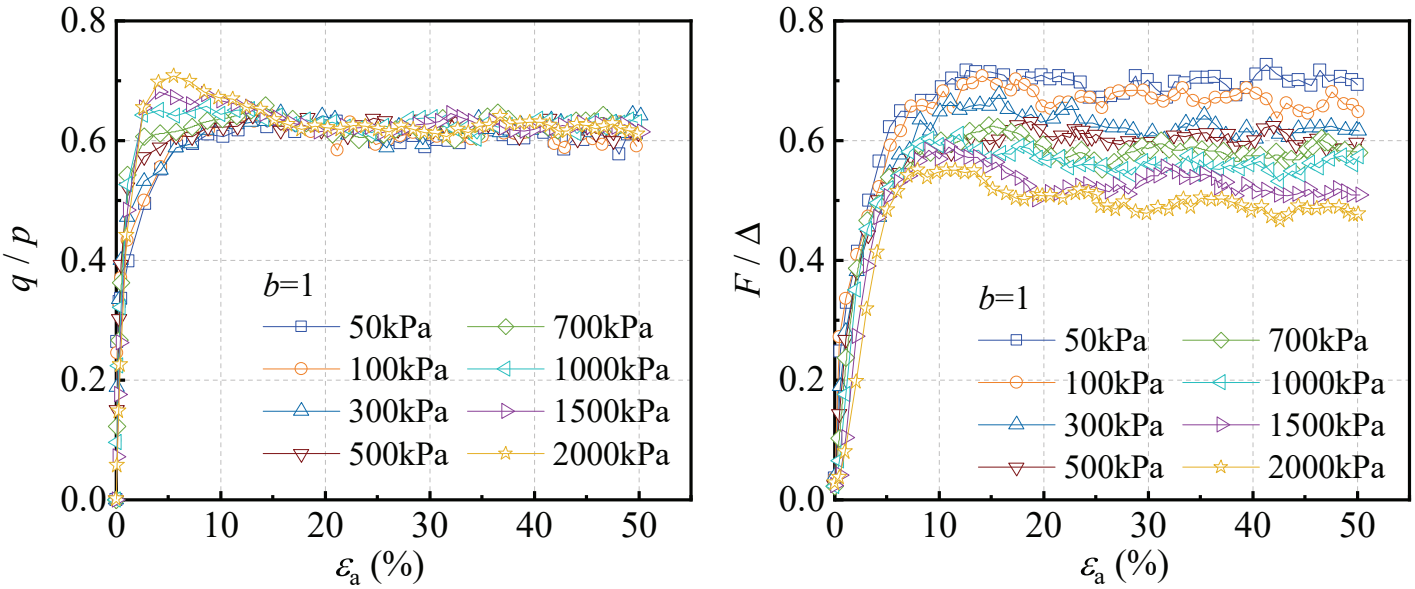
0.8
0.6
0.4
0.2
0.0
q / p
b=1
50kPa
100kPa
300kPa
500kPa
700kPa
1000kPa
1500kPa
2000kPa
0
10
20
30
40
50
εa (%)
F / Δ

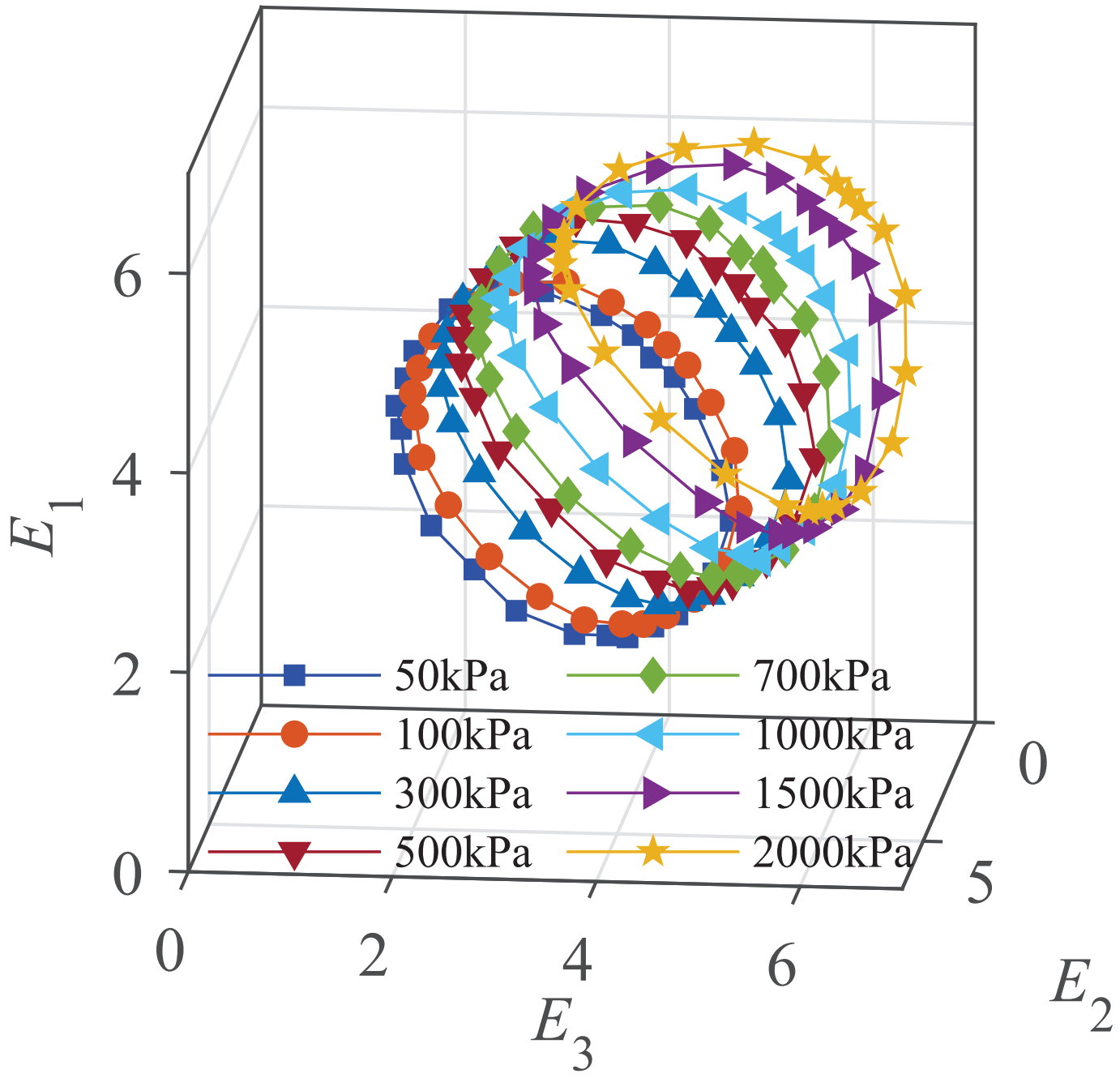
E_1
6
4
2
0
0
2
4
6
E_3
0
5
E_2
50kPa
100kPa
300kPa
500kPa
700kPa
1000kPa
1500kPa
2000kPa

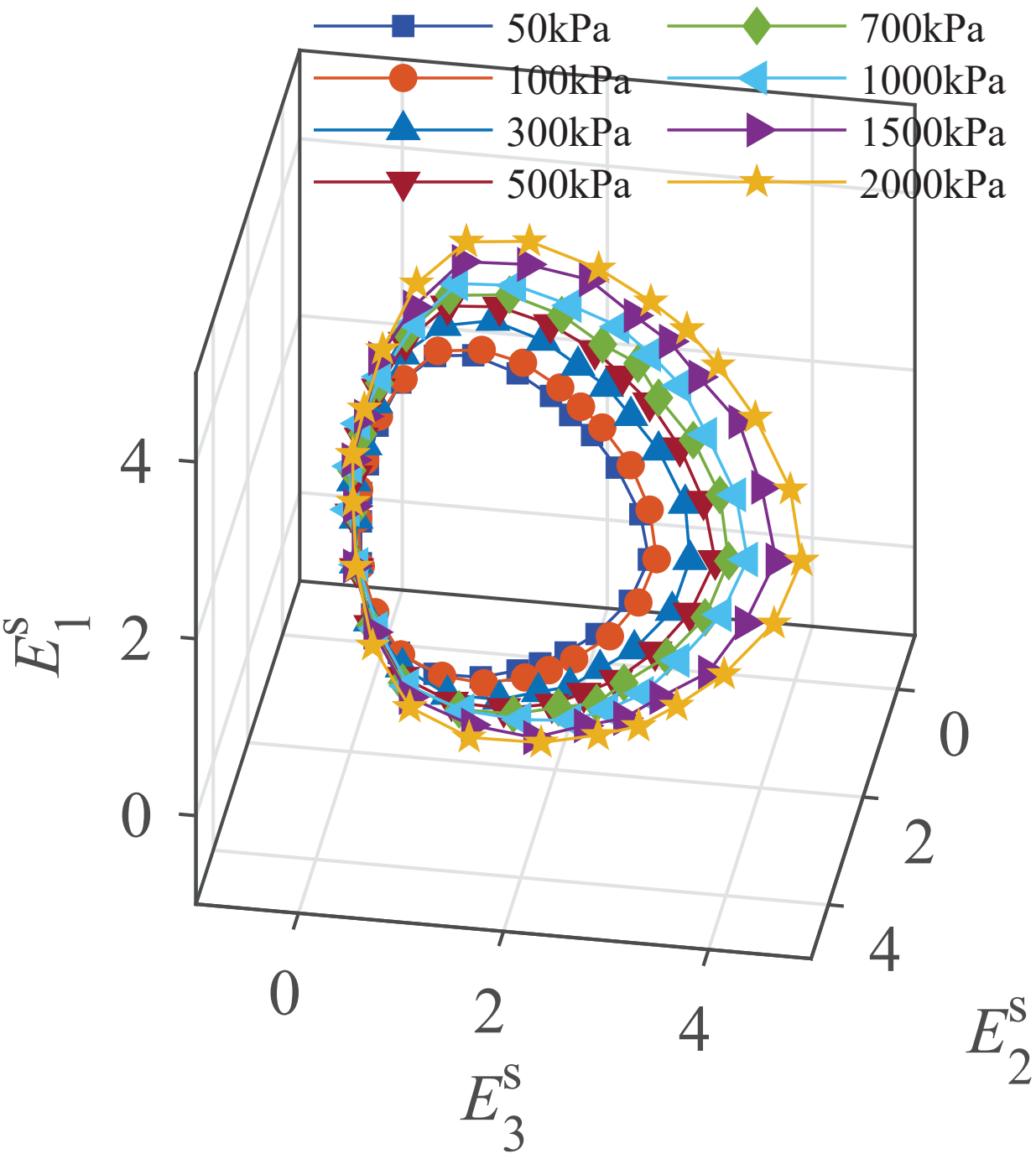
50kPa
100kPa
300kPa
500kPa
700kPa
1000kPa
1500kPa
2000kPa
E_1^S
E_2^S
E_3^S
0
2
4

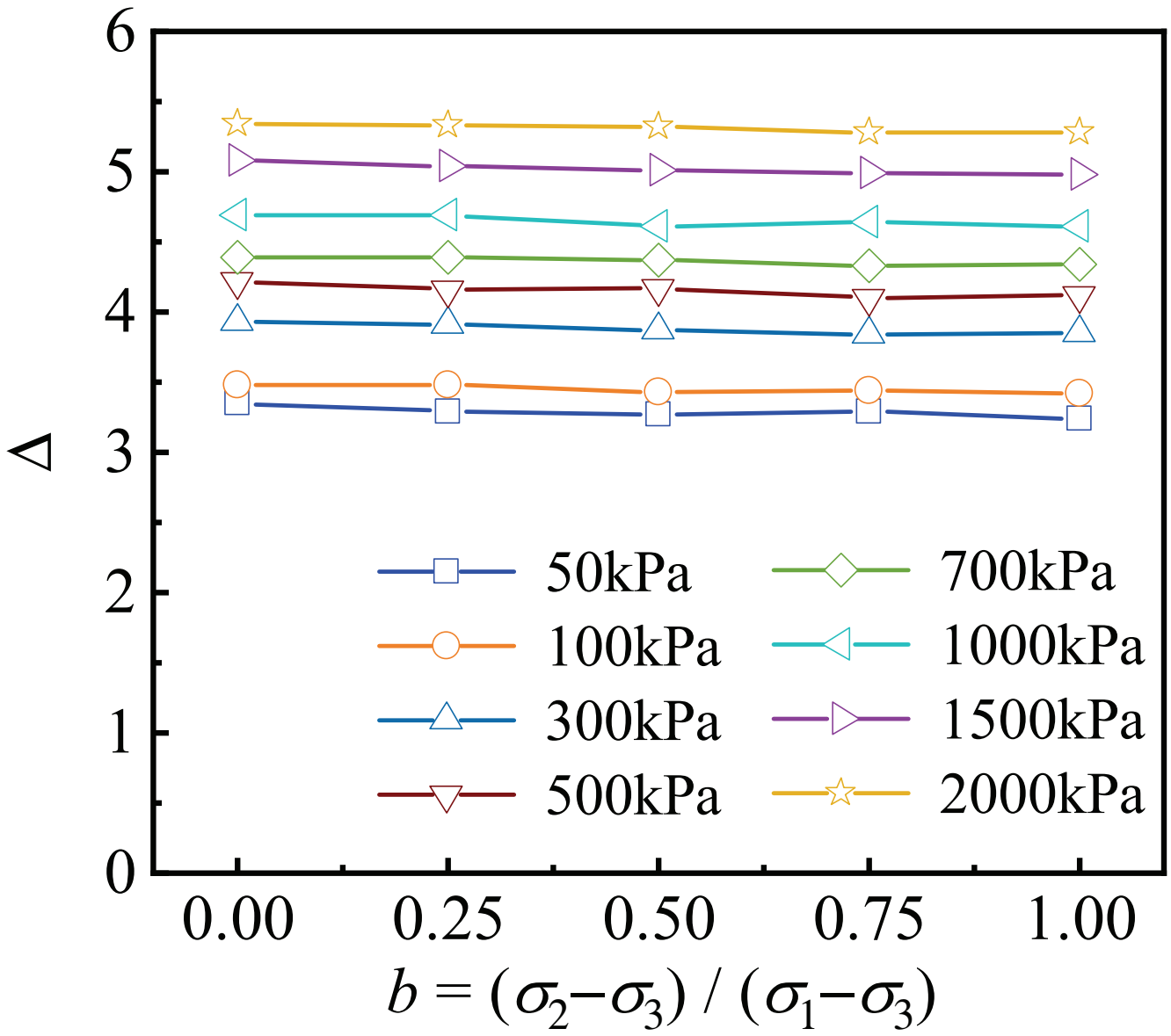
6
5
4
3
2
1
0
Δ
0.00
0.25
0.50
0.75
1.00
$b = (\sigma_2 - \sigma_3) / (\sigma_1 - \sigma_3)$
50kPa
100kPa
300kPa
500kPa
700kPa
1000kPa
1500kPa
2000kPa

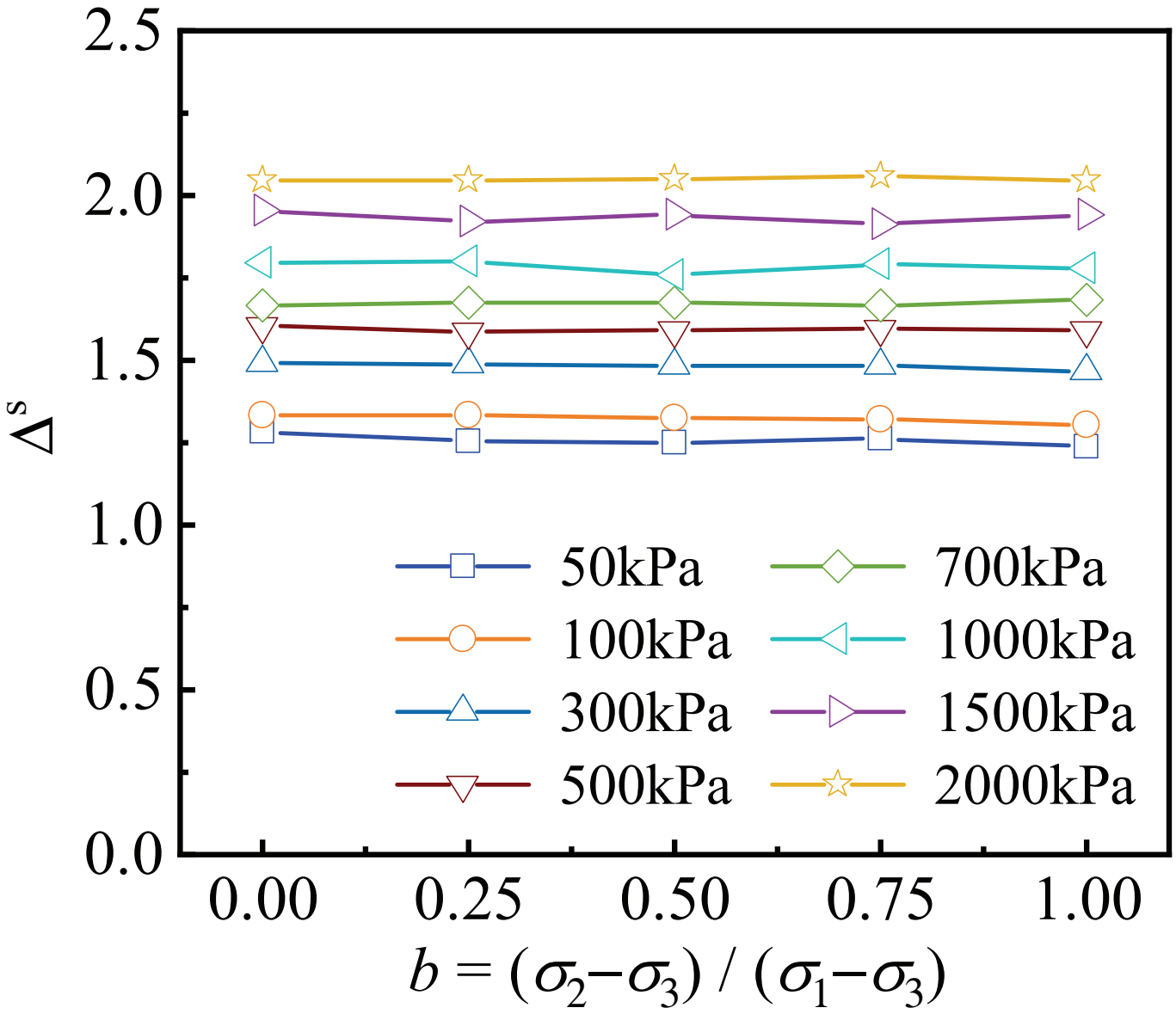
2.5
2.0
1.5
1.0
0.5
0.0
Δ^s
0.00
0.25
0.50
0.75
1.00
$b = (\sigma_2 - \sigma_3) / (\sigma_1 - \sigma_3)$
50kPa
100kPa
300kPa
500kPa
700kPa
1000kPa
1500kPa
2000kPa

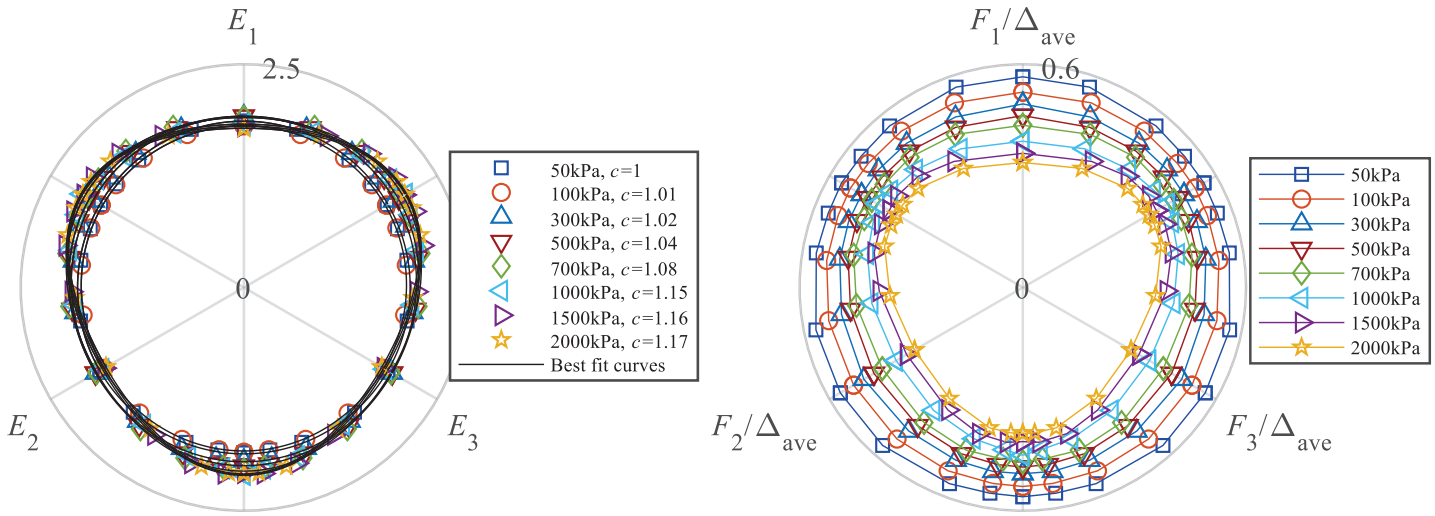
E_1
2.5
0
E_2
E_3
50kPa, c=1
100kPa, c=1.01
300kPa, c=1.02
500kPa, c=1.04
700kPa, c=1.08
1000kPa, c=1.15
1500kPa, c=1.16
2000kPa, c=1.17
Best fit curves
F_1/Δ_{ave}
0.6
0
F_2/Δ_{ave}
F_3/Δ_{ave}
50kPa
100kPa
300kPa
500kPa
700kPa
1000kPa
1500kPa
2000kPa

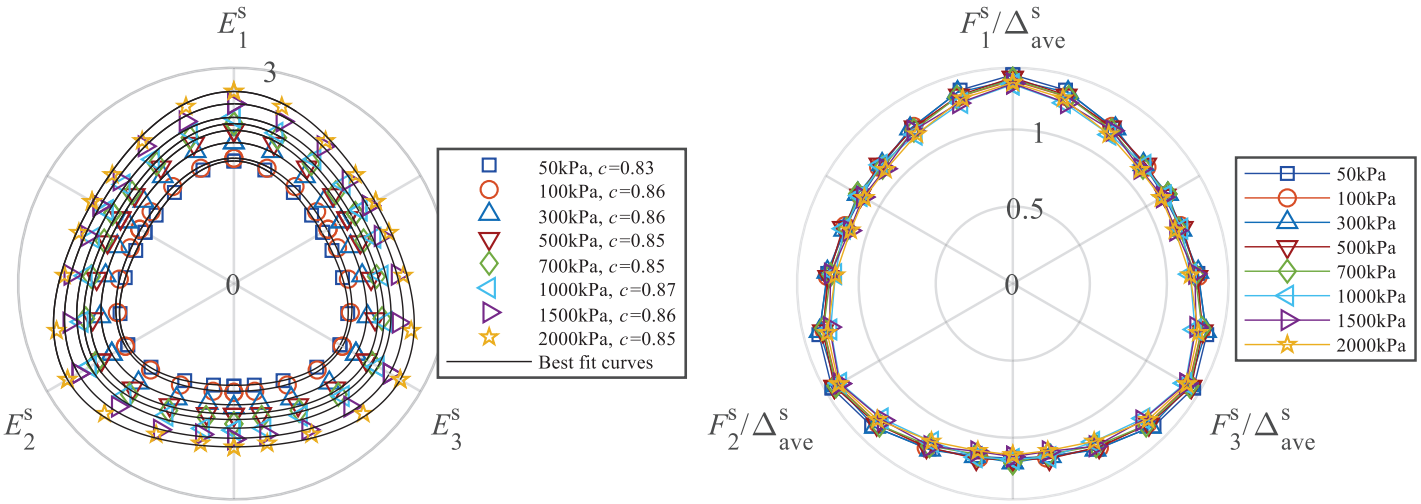
E_1^s
3
0
E_2^s
E_3^s
50kPa, c=0.83
100kPa, c=0.86
300kPa, c=0.86
500kPa, c=0.85
700kPa, c=0.85
1000kPa, c=0.87
1500kPa, c=0.86
2000kPa, c=0.85
Best fit curves
F_1^s/Δ_{ave}^s
1
0.5
0
F_2^s/Δ_{ave}^s
F_3^s/Δ_{ave}^s
50kPa
100kPa
300kPa
500kPa
700kPa
1000kPa
1500kPa
2000kPa

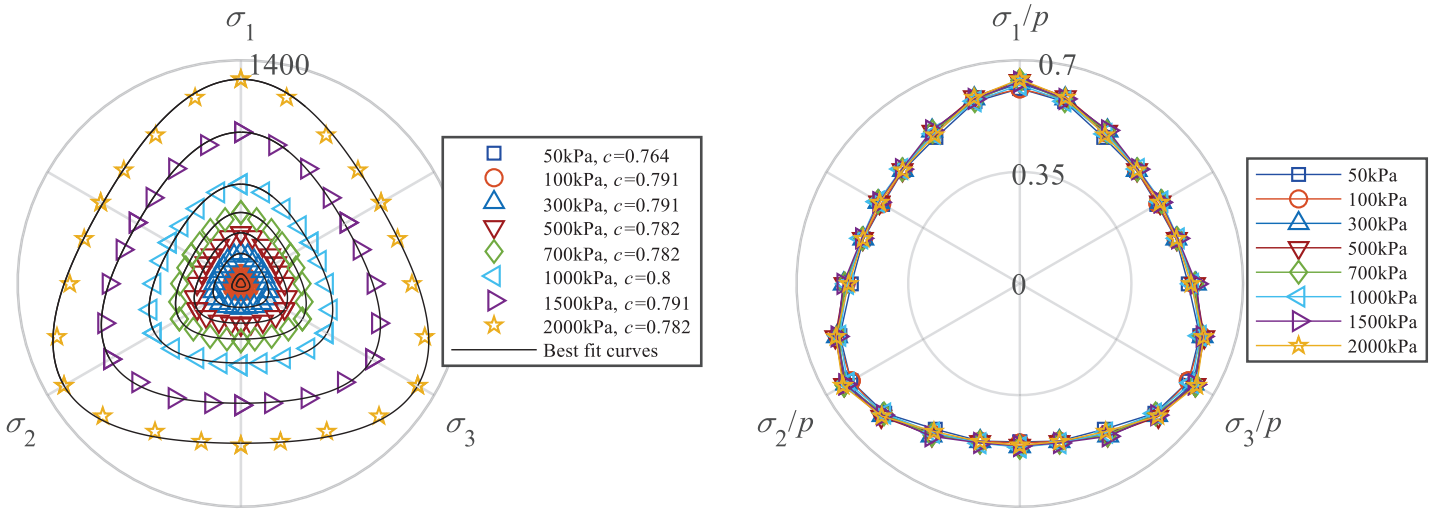
σ_1
1400
σ_2
σ_3
50kPa, c=0.764
100kPa, c=0.791
300kPa, c=0.791
500kPa, c=0.782
700kPa, c=0.782
1000kPa, c=0.8
1500kPa, c=0.791
2000kPa, c=0.782
Best fit curves
σ_1/p
0.7
0.35
0
σ_2/p
σ_3/p
50kPa
100kPa
300kPa
500kPa
700kPa
1000kPa
1500kPa
2000kPa

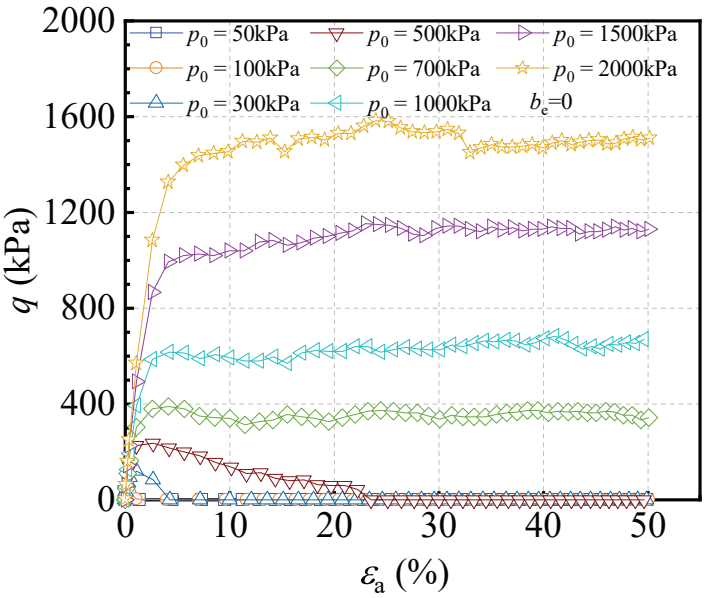
2000
1600
1200
800
400
0
q (kPa)
0
10
20
30
40
50
ε_a (%)
p_0 = 50kPa
p_0 = 100kPa
p_0 = 300kPa
p_0 = 500kPa
p_0 = 700kPa
p_0 = 1000kPa
p_0 = 1500kPa
p_0 = 2000kPa
b_e=0

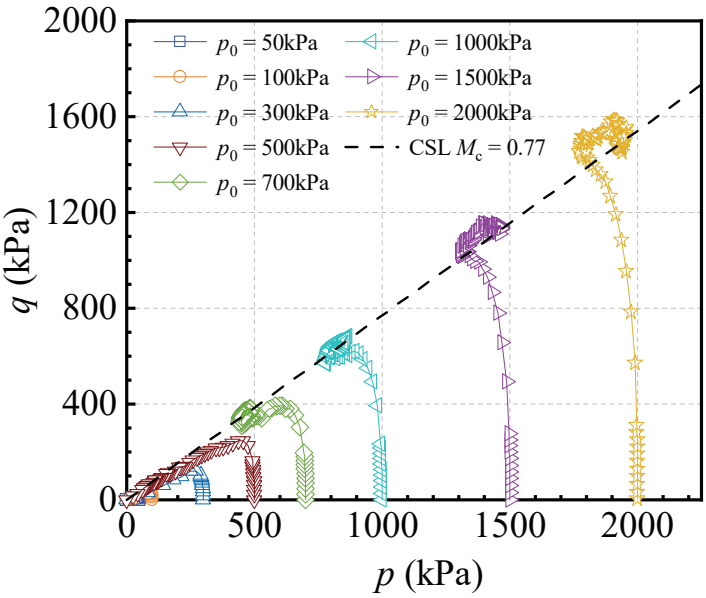
2000
1600
1200
800
400
0
q (kPa)
0
500
1000
1500
2000
p (kPa)
p_0 = 50kPa
p_0 = 100kPa
p_0 = 300kPa
p_0 = 500kPa
p_0 = 700kPa
p_0 = 1000kPa
p_0 = 1500kPa
p_0 = 2000kPa
CSL M_c = 0.77

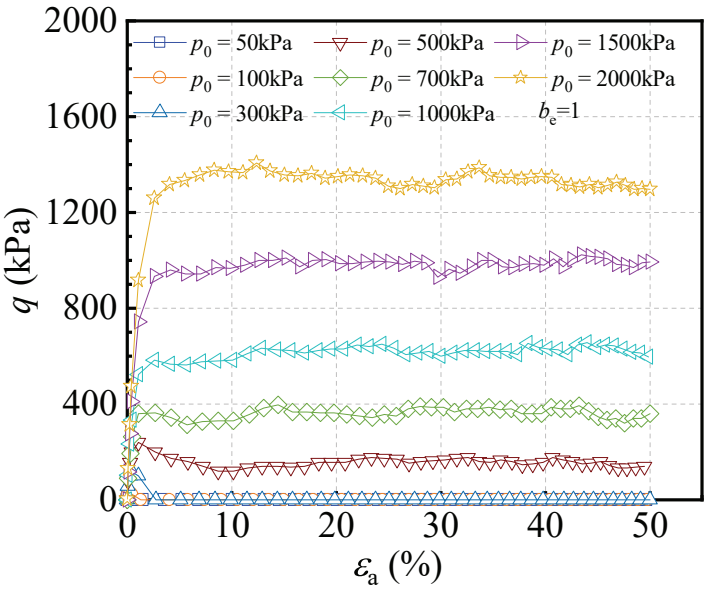
2000
1600
1200
800
400
0
q (kPa)
0
10
20
30
40
50
ε_a (%)
p_0 = 50kPa
p_0 = 100kPa
p_0 = 300kPa
p_0 = 500kPa
p_0 = 700kPa
p_0 = 1000kPa
p_0 = 1500kPa
p_0 = 2000kPa
b_e=1

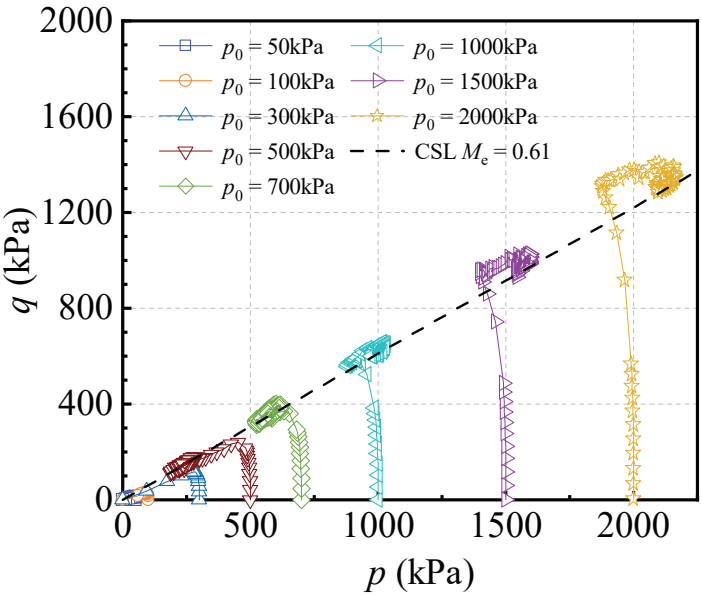
2000
1600
1200
800
400
0
q (kPa)
0
500
1000
1500
2000
p (kPa)
p_0 = 50kPa
p_0 = 100kPa
p_0 = 300kPa
p_0 = 500kPa
p_0 = 700kPa
p_0 = 1000kPa
p_0 = 1500kPa
p_0 = 2000kPa
CSL M_e = 0.61

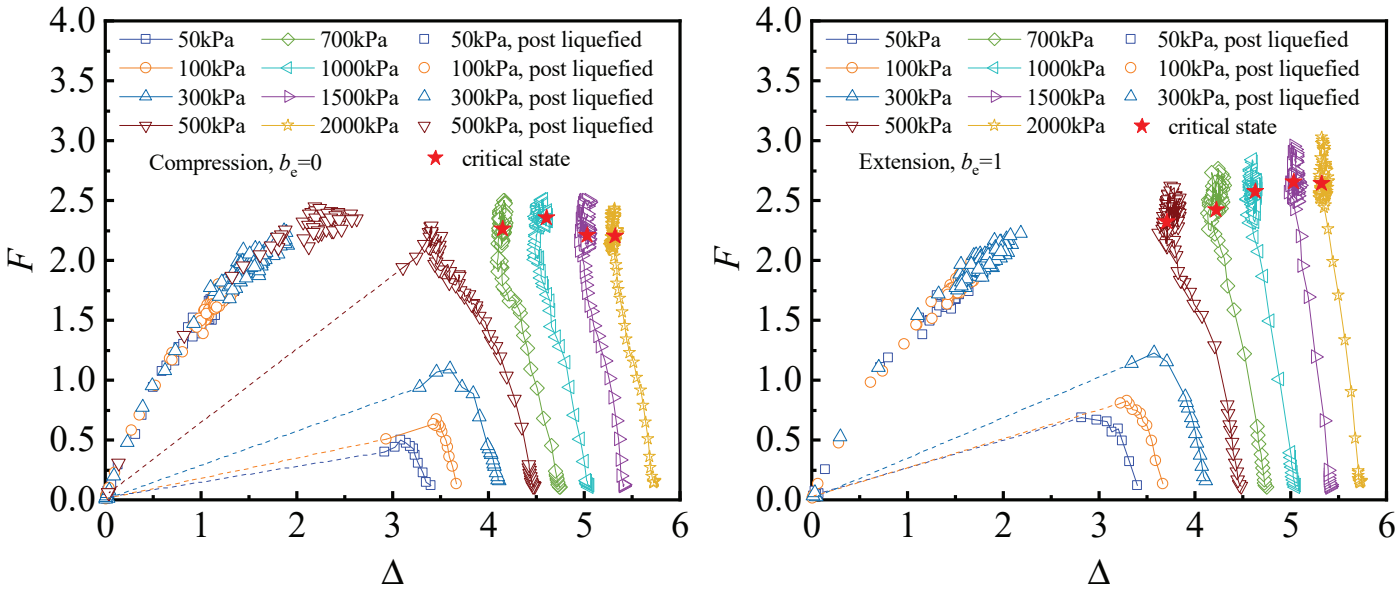
50kPa
100kPa
300kPa
500kPa
700kPa
1000kPa
1500kPa
2000kPa
50kPa, post liquefied
100kPa, post liquefied
300kPa, post liquefied
500kPa, post liquefied
critical state
Compression, b_e=0
Extension, b_e=1
F
Δ
0.0
0.5
1.0
1.5
2.0
2.5
3.0
3.5
4.0
0
1
2
3
4
5
6

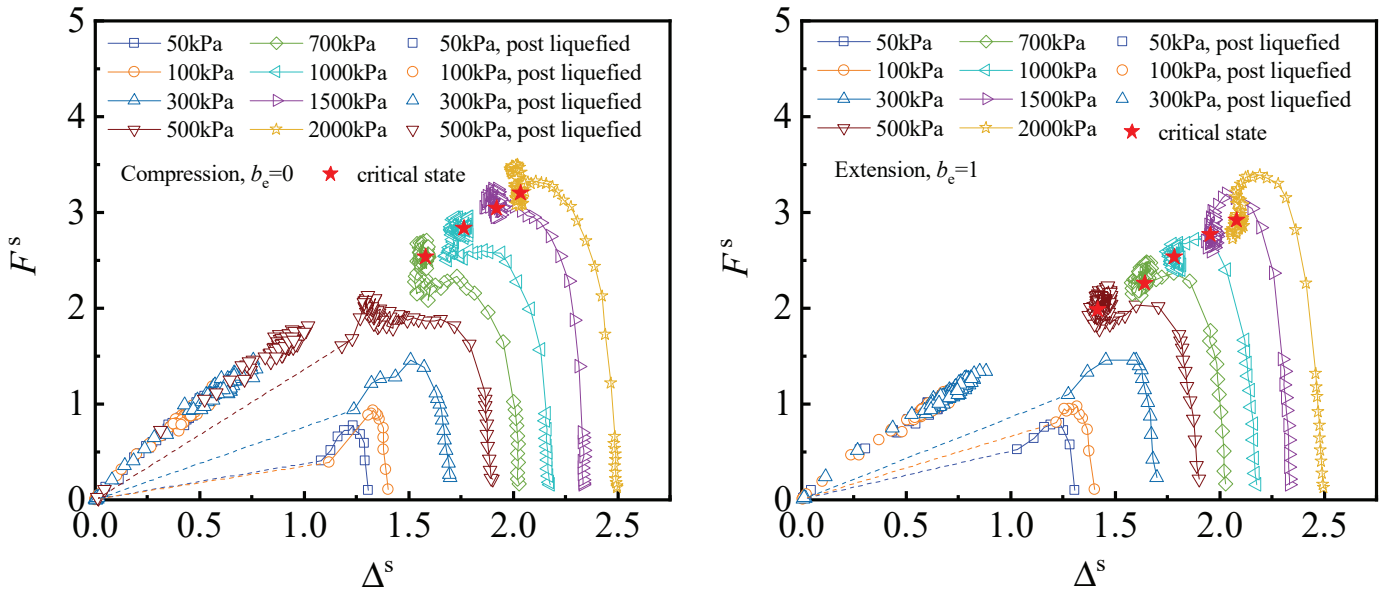
50kPa
100kPa
300kPa
500kPa
700kPa
1000kPa
1500kPa
2000kPa
50kPa, post liquefied
100kPa, post liquefied
300kPa, post liquefied
500kPa, post liquefied
Compression, b_e=0
critical state
Extension, b_e=1
F^s
Δ^s
0.0
0.5
1.0
1.5
2.0
2.5
0
1
2
3
4
5

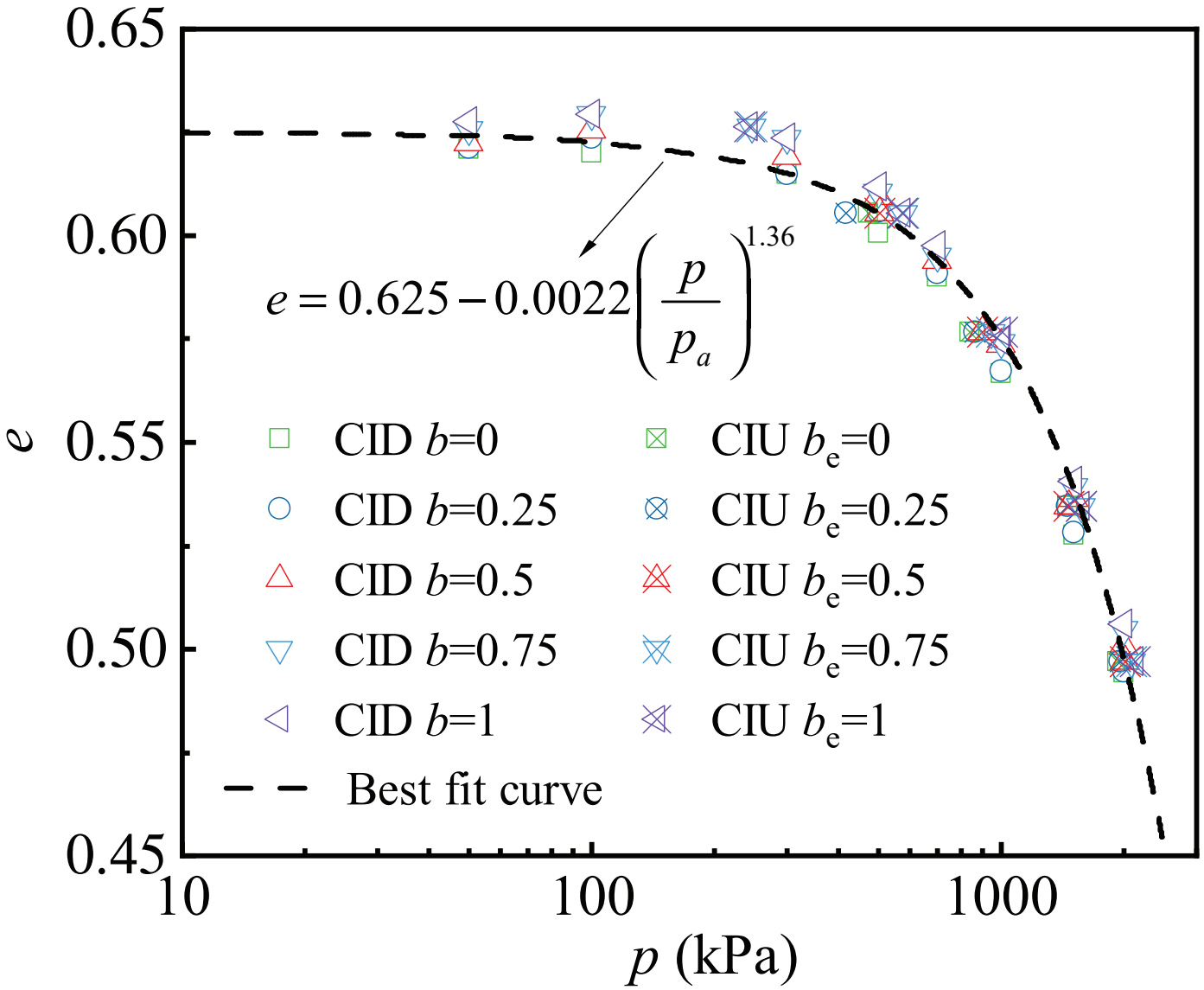
0.65
0.60
0.55
0.50
0.45
e
10
100
1000
p (kPa)
e = 0.625 − 0.0022 (p / p_a)^1.36
CID b=0
CID b=0.25
CID b=0.5
CID b=0.75
CID b=1
CIU b_e=0
CIU b_e=0.25
CIU b_e=0.5
CIU b_e=0.75
CIU b_e=1
Best fit curve

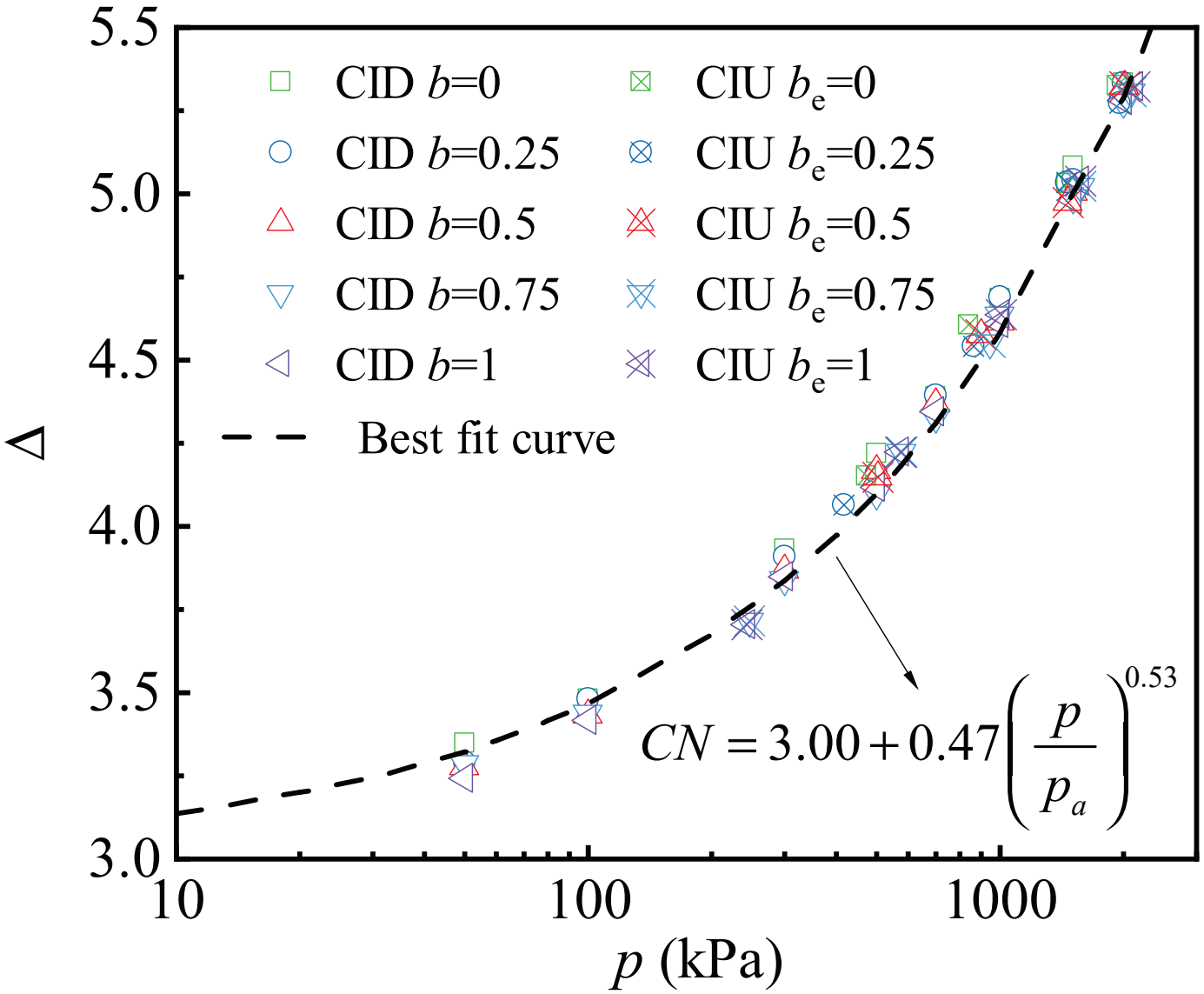
5.5
5.0
4.5
4.0
3.5
3.0
Δ
10
100
1000
p (kPa)
CID b=0
CID b=0.25
CID b=0.5
CID b=0.75
CID b=1
CIU b_e=0
CIU b_e=0.25
CIU b_e=0.5
CIU b_e=0.75
CIU b_e=1
Best fit curve
CN = 3.00 + 0.47 (p / p_a)^0.53

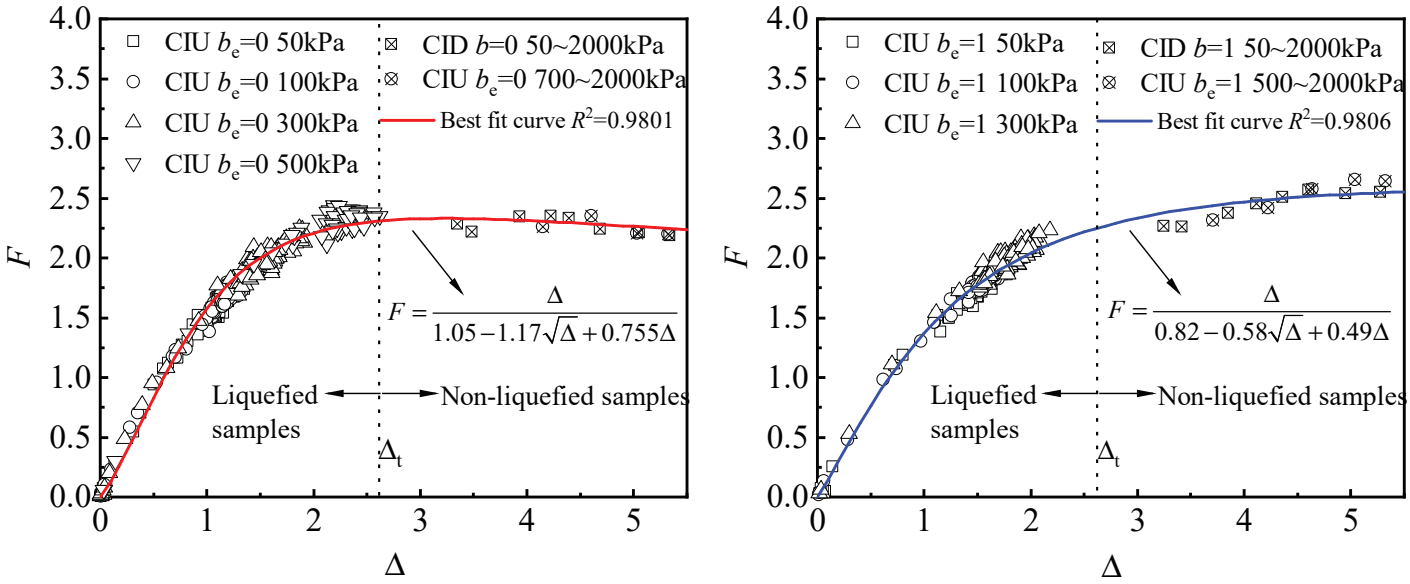
CIU b_e=0 50kPa
CIU b_e=0 100kPa
CIU b_e=0 300kPa
CIU b_e=0 500kPa
CID b=0 50~2000kPa
CIU b_e=0 700~2000kPa
Best fit curve R^2=0.9801
$F=\frac{\Delta}{1.05-1.17\sqrt{\Delta}+0.755\Delta}$
Liquefied samples
Non-liquefied samples
Δ_t
F
Δ
CIU b_e=1 50kPa
CIU b_e=1 100kPa
CIU b_e=1 300kPa
CID b=1 50~2000kPa
CIU b_e=1 500~2000kPa
Best fit curve R^2=0.9806
$F=\frac{\Delta}{0.82-0.58\sqrt{\Delta}+0.49\Delta}$
Liquefied samples
Non-liquefied samples
Δ_t
F
Δ

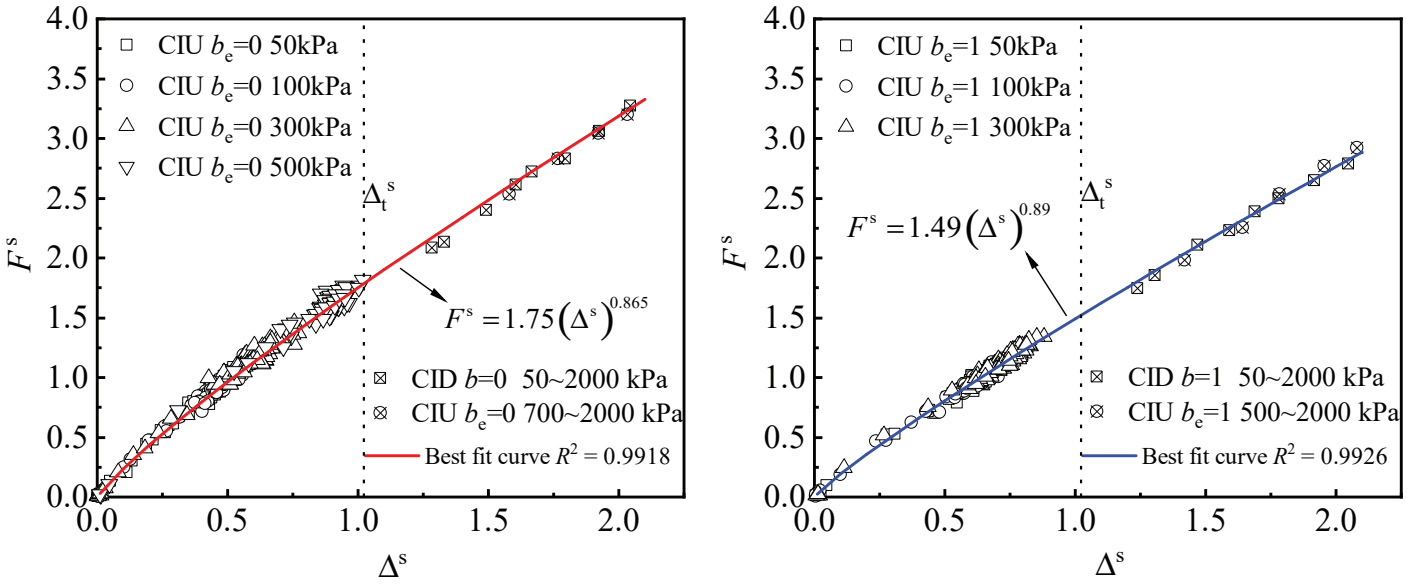
CIU b_e=0 50kPa
CIU b_e=0 100kPa
CIU b_e=0 300kPa
CIU b_e=0 500kPa
Δ_t^s
$F^s = 1.75(\Delta^s)^{0.865}$
CID b=0 50~2000 kPa
CIU b_e=0 700~2000 kPa
Best fit curve R^2 = 0.9918
F^s
Δ^s
CIU b_e=1 50kPa
CIU b_e=1 100kPa
CIU b_e=1 300kPa
Δ_t^s
$F^s = 1.49(\Delta^s)^{0.89}$
CID b=1 50~2000 kPa
CIU b_e=1 500~2000 kPa
Best fit curve R^2 = 0.9926
F^s
Δ^s

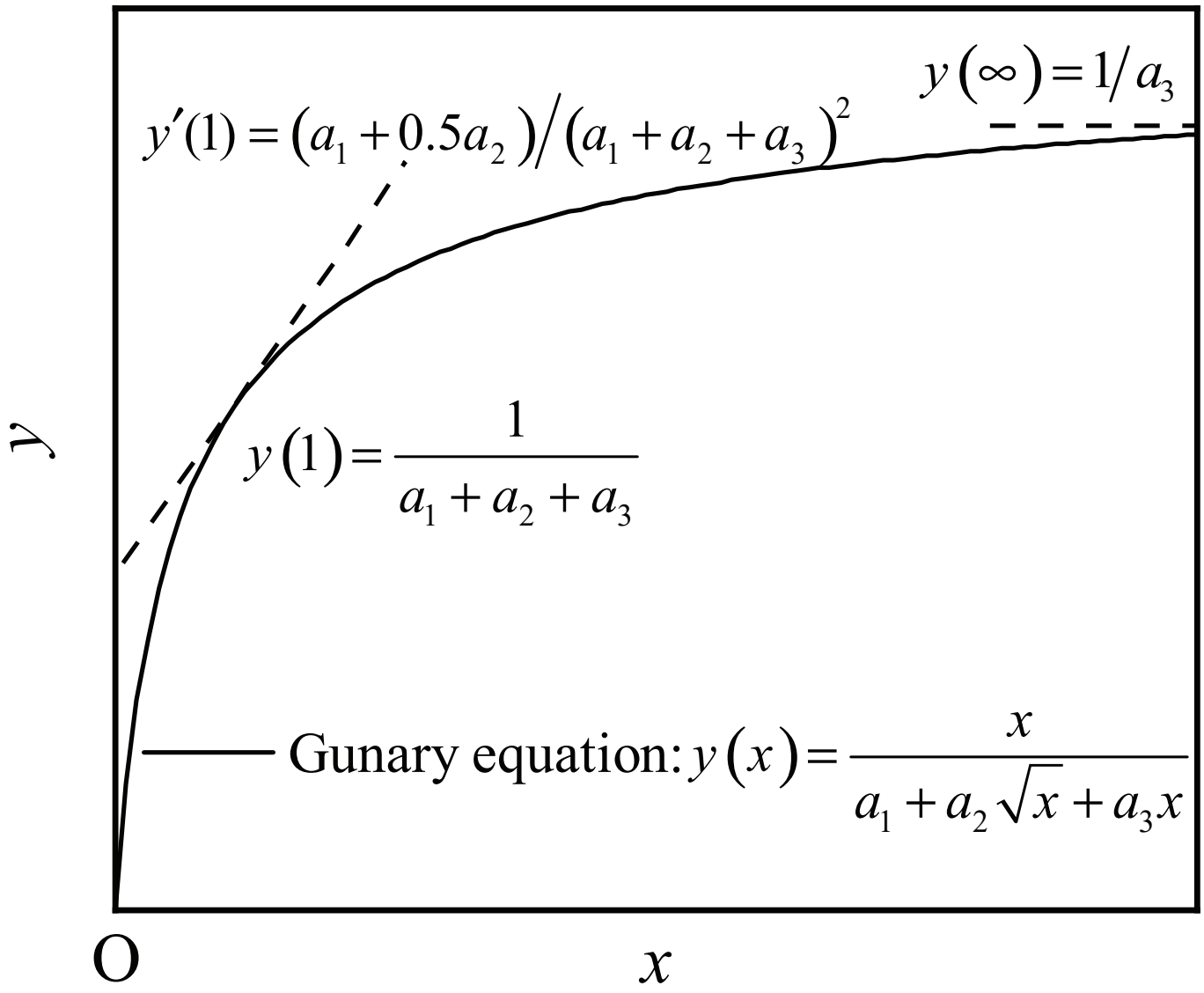
$y(\infty)=1/a_3$
$y'(1)=(a_1+0.5a_2)/(a_1+a_2+a_3)^2$
y
$y(1)=\dfrac{1}{a_1+a_2+a_3}$
Gunary equation: $y(x)=\dfrac{x}{a_1+a_2\sqrt{x}+a_3x}$
O
x

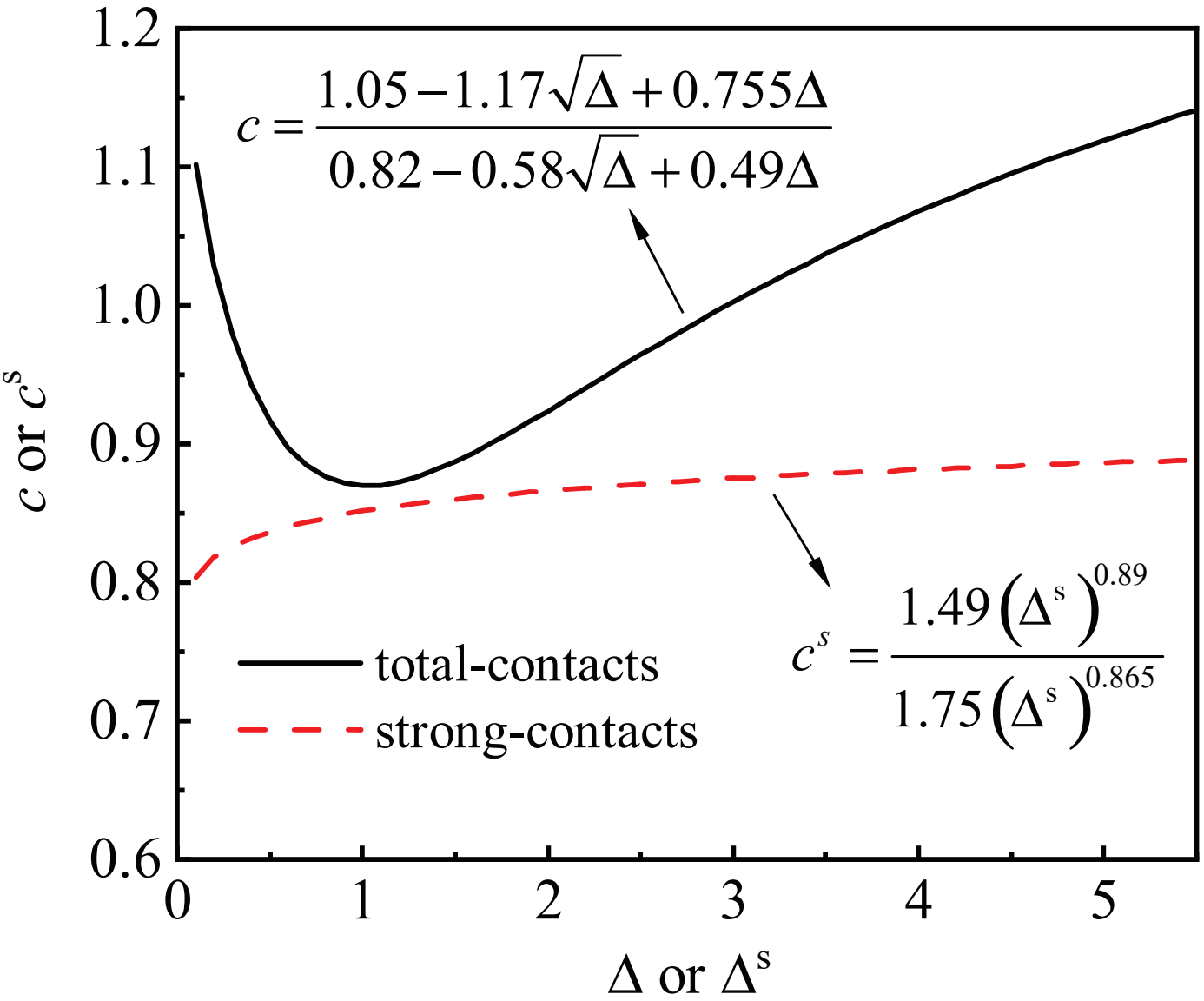
1.2
1.1
1.0
0.9
0.8
0.7
0.6
0
1
2
3
4
5
c or c^s
Δ or Δ^s
c = (1.05 − 1.17√Δ + 0.755Δ) / (0.82 − 0.58√Δ + 0.49Δ)
c^s = 1.49(Δ^s)^0.89 / 1.75(Δ^s)^0.865
total-contacts
strong-contacts

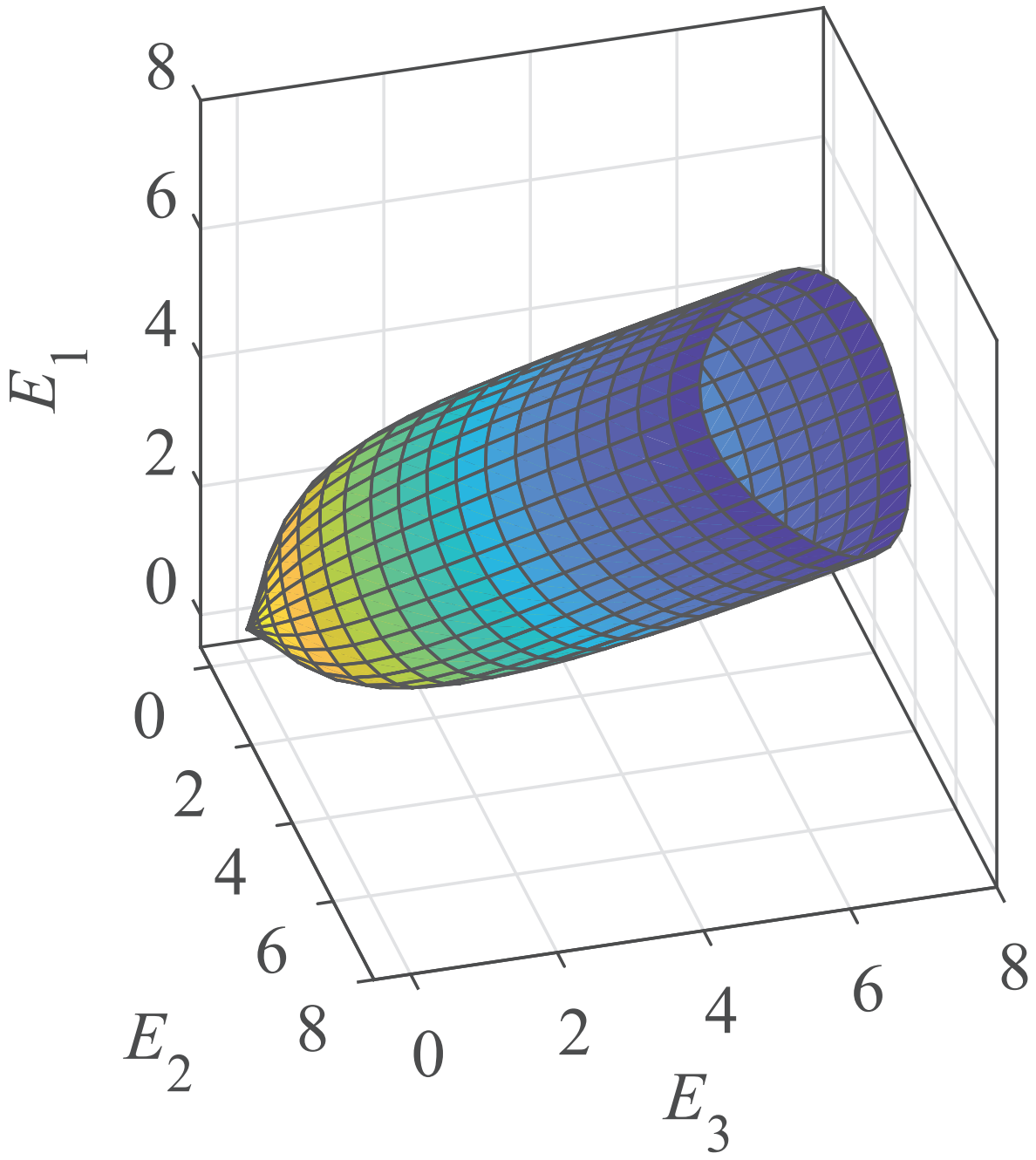
8
6
4
2
0
E_1
0
2
4
6
8
E_2
0
2
4
6
8
E_3

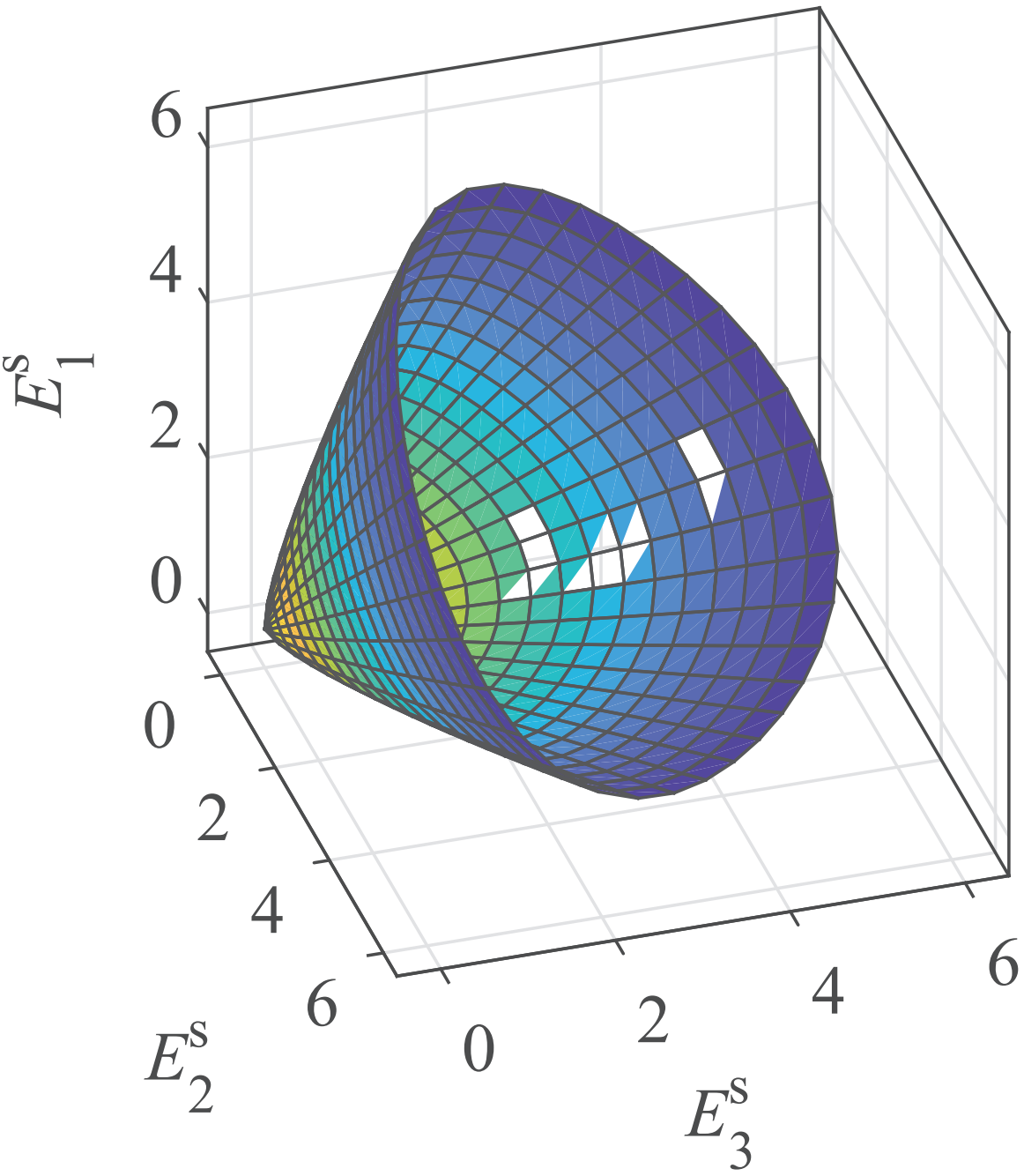
6
4
2
0
E_1^s
0
2
4
6
E_2^s
0
2
4
6
E_3^s

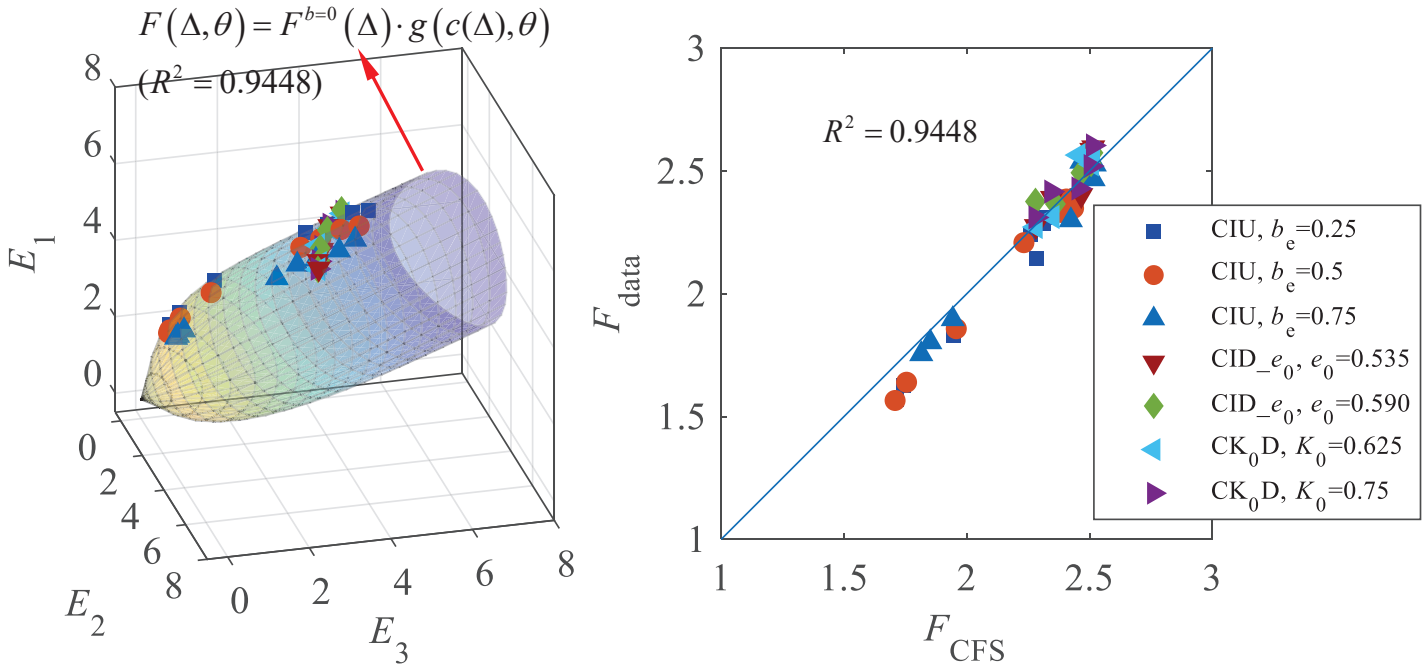
$F(\Delta,\theta)=F^{b=0}(\Delta)\cdot g(c(\Delta),\theta)$
($R^2=0.9448$)
E_1
E_2
E_3
$R^2=0.9448$
F_{data}
F_{CFS}
CIU, b_e=0.25
CIU, b_e=0.5
CIU, b_e=0.75
CID_e_0, e_0=0.535
CID_e_0, e_0=0.590
CK_0D, K_0=0.625
CK_0D, K_0=0.75

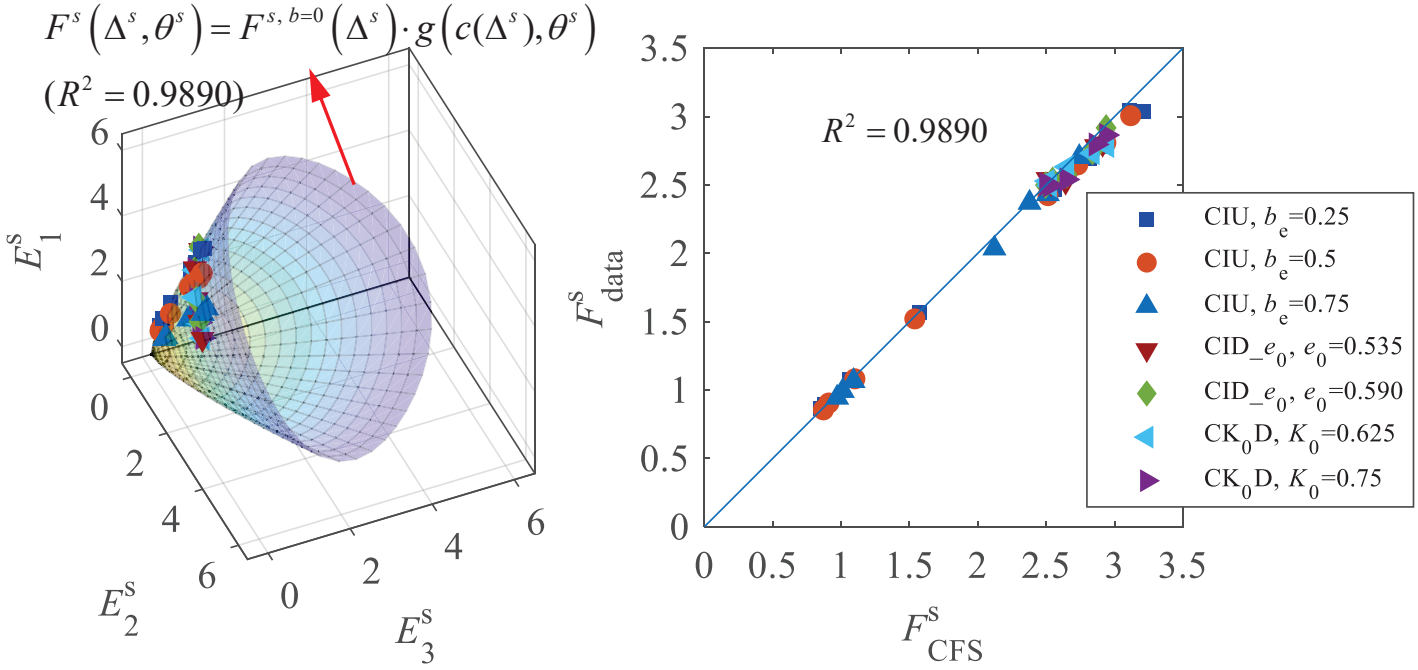
$F^s\left(\Delta^s,\theta^s\right)=F^{s,\,b=0}\left(\Delta^s\right)\cdot g\left(c(\Delta^s),\theta^s\right)$
$(R^2=0.9890)$
E_1^s
E_2^s
E_3^s
$R^2=0.9890$
F_{data}^s
F_{CFS}^s
CIU, b_e=0.25
CIU, b_e=0.5
CIU, b_e=0.75
CID_e_0, e_0=0.535
CID_e_0, e_0=0.590
CK_0D, K_0=0.625
CK_0D, K_0=0.75

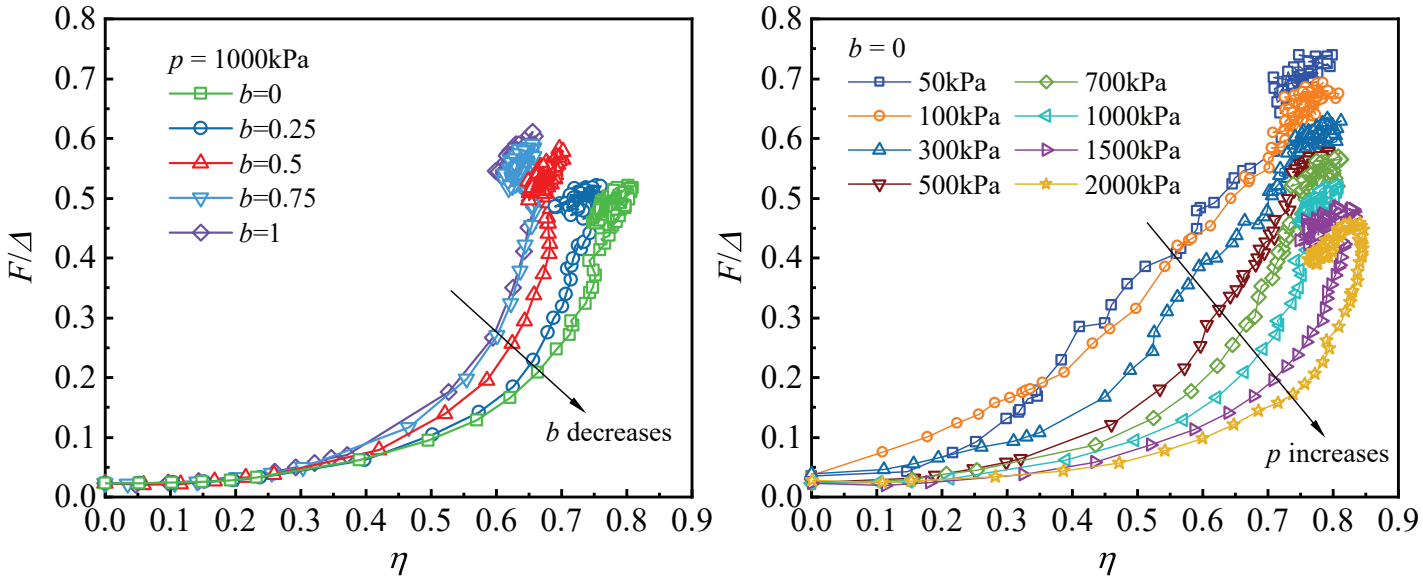
p = 1000kPa
b=0
b=0.25
b=0.5
b=0.75
b=1
b decreases
F/Δ
η
b = 0
50kPa
100kPa
300kPa
500kPa
700kPa
1000kPa
1500kPa
2000kPa
p increases
F/Δ
η

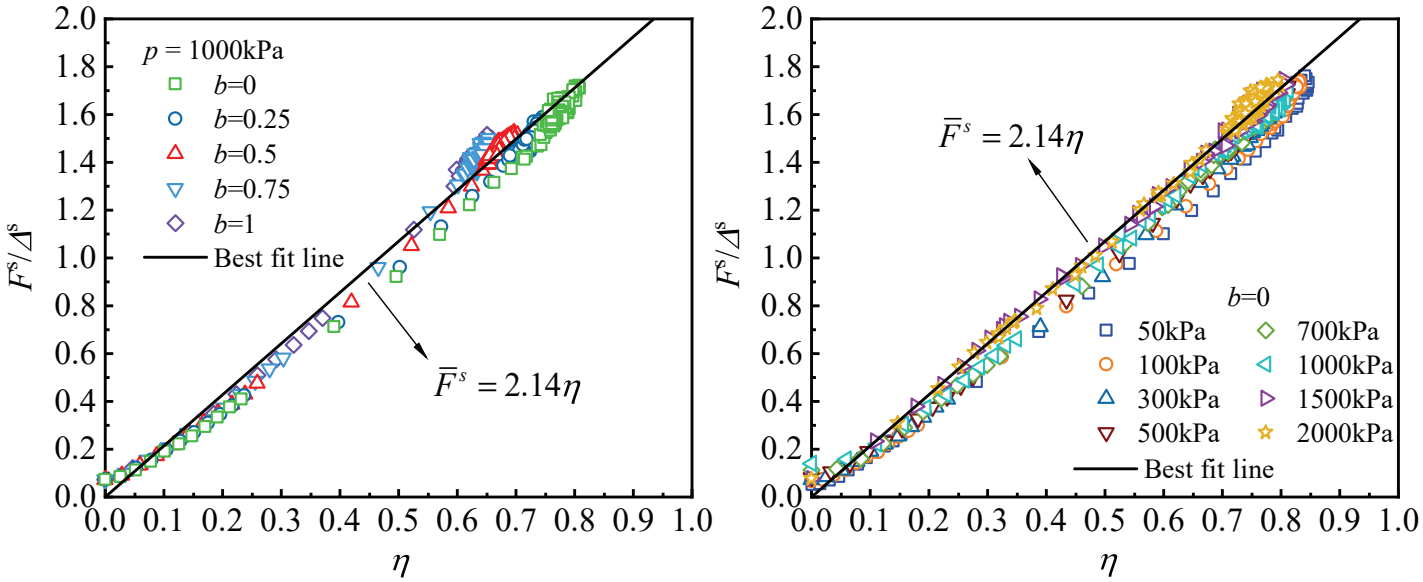
p = 1000kPa
b=0
b=0.25
b=0.5
b=0.75
b=1
Best fit line
$\bar{F}^s = 2.14\eta$
F^s/Δ^s
η
b=0
50kPa
100kPa
300kPa
500kPa
700kPa
1000kPa
1500kPa
2000kPa
Best fit line
$\bar{F}^s = 2.14\eta$
F^s/Δ^s
η

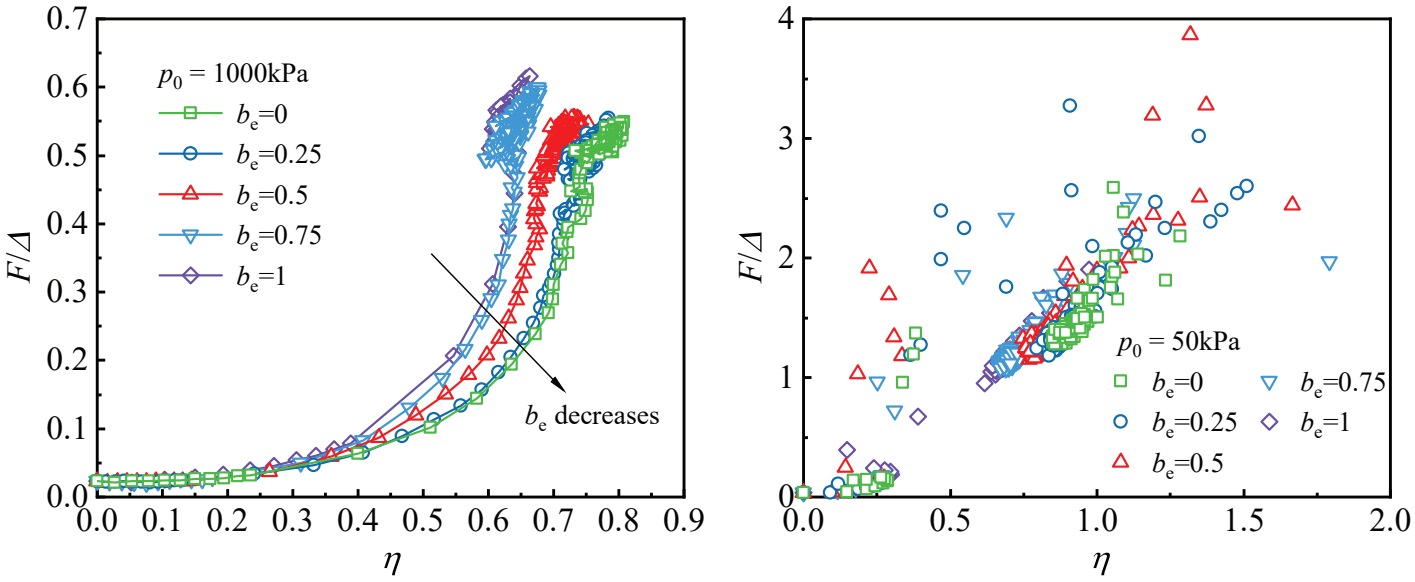
p_0 = 1000kPa
b_e=0
b_e=0.25
b_e=0.5
b_e=0.75
b_e=1
b_e decreases
F/Δ
η
p_0 = 50kPa
b_e=0
b_e=0.25
b_e=0.5
b_e=0.75
b_e=1
F/Δ
η

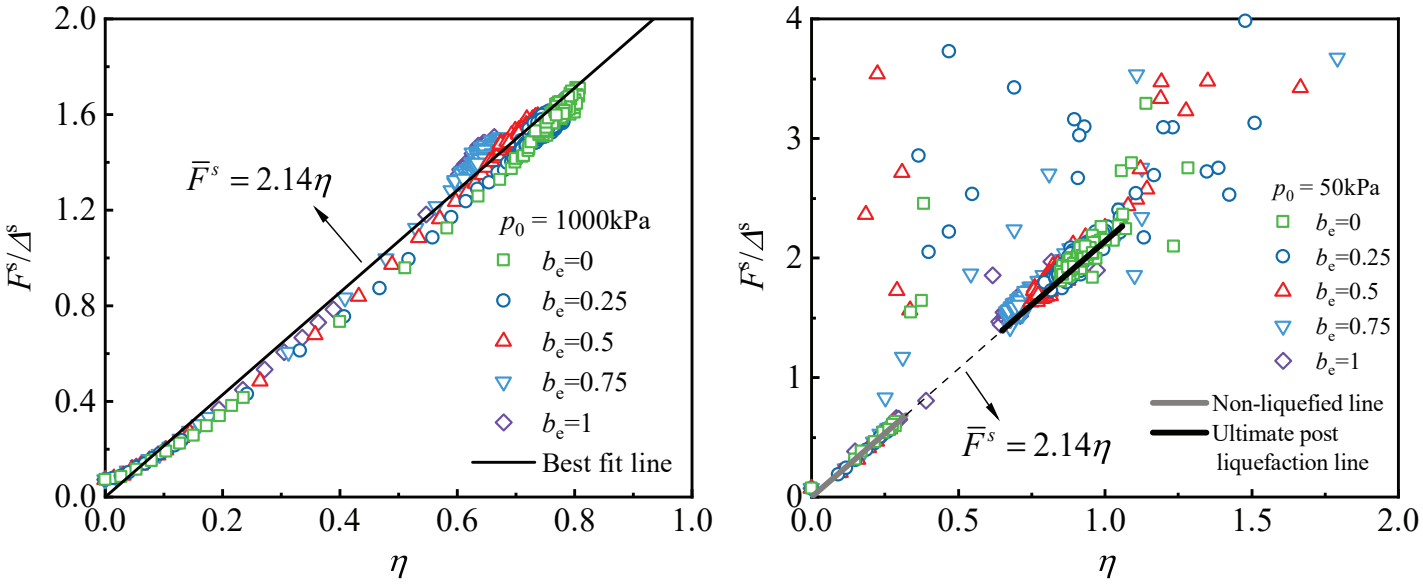
2.0
1.6
1.2
0.8
0.4
0.0
0.0
0.2
0.4
0.6
0.8
1.0
F^s/Δ^s
η
$\overline{F}^s = 2.14\eta$
p_0 = 1000kPa
b_e=0
b_e=0.25
b_e=0.5
b_e=0.75
b_e=1
Best fit line
4
3
2
1
0
0.0
0.5
1.0
1.5
2.0
F^s/Δ^s
η
$\overline{F}^s = 2.14\eta$
p_0 = 50kPa
b_e=0
b_e=0.25
b_e=0.5
b_e=0.75
b_e=1
Non-liquefied line
Ultimate post liquefaction line

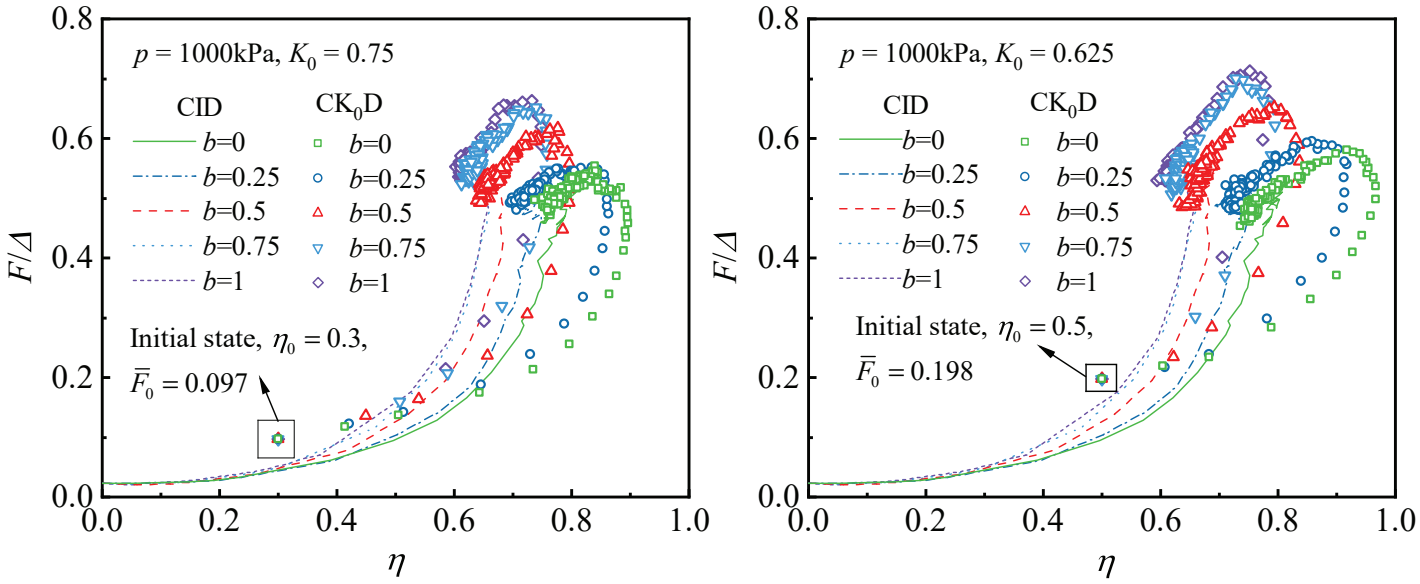
p = 1000kPa, K0 = 0.75
CID
CK0D
b=0
b=0.25
b=0.5
b=0.75
b=1
Initial state, η0 = 0.3,
F̄0 = 0.097
F/Δ
η
p = 1000kPa, K0 = 0.625
Initial state, η0 = 0.5,
F̄0 = 0.198

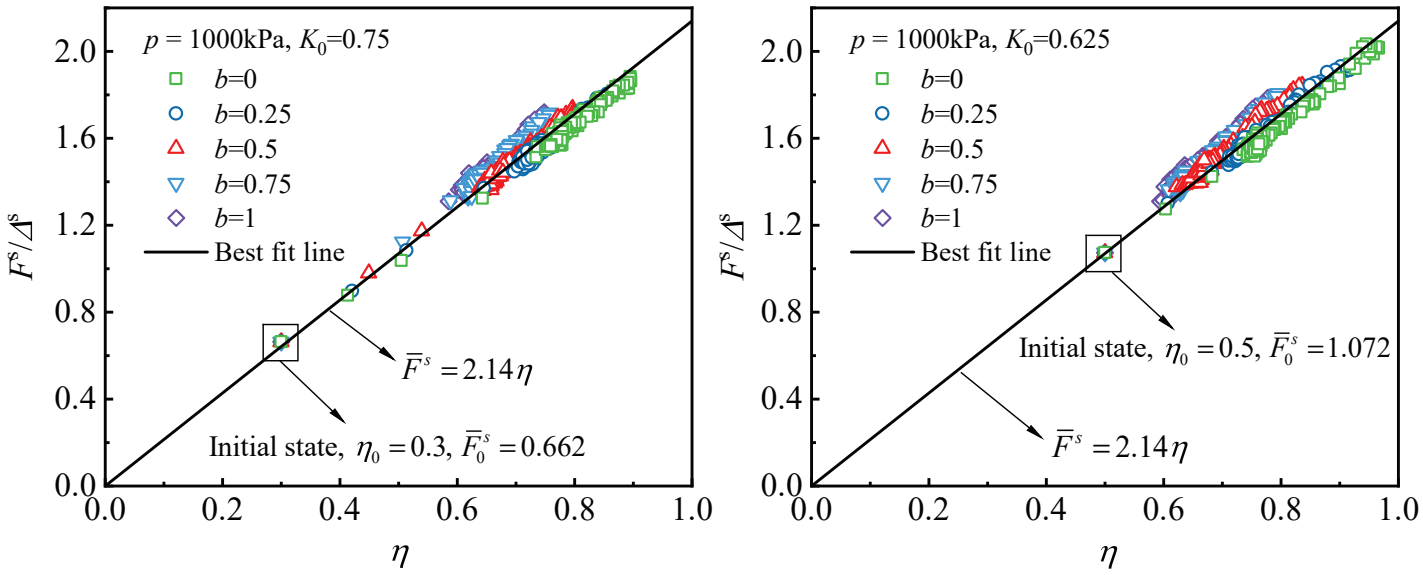
p = 1000kPa, K0=0.75
b=0
b=0.25
b=0.5
b=0.75
b=1
Best fit line
F̄s =2.14η
Initial state, η0 =0.3, F̄0s =0.662
Fs/Δs
η
p = 1000kPa, K0=0.625
b=0
b=0.25
b=0.5
b=0.75
b=1
Best fit line
Initial state, η0 =0.5, F̄0s =1.072
F̄s =2.14η
Fs/Δs
η